Canadian Science Publishing | Canadian Geotechnical Journal

Dynamic, In-situ, Nonlinear-Inelastic Response and Post-Cyclic Strength of a Plastic Silt Deposit

Journal:	*Canadian Geotechnical Journal*
Manuscript ID	cgj-2020-0652.R2
Manuscript Type:	Article
Date Submitted by the Author:	n/a
Complete List of Authors:	Jana, Amalesh; Oregon State University Stuedlein, Armin; Oregon State University, School of Civil and Construction Engineering
Keyword:	shear modulus degradation, excess pore pressure generation, in-situ testing, controlled blasting, soil dynamics
Is the invited manuscript for consideration in a Special Issue? :	Not applicable (regular submission)

SCHOLARONE™
Manuscripts

Dynamic, *In-situ*, Nonlinear-Inelastic Response and Post-Cyclic Strength of a Plastic Silt Deposit

Amalesh Jana[1] and Armin W. Stuedlein[2]

[1] Graduate Research Assistant, 101 Kearney Hall, School of Civil and Construction Engineering, Oregon State University, Corvallis, OR 97331

[2] Professor, 101 Kearney Hall, School of Civil and Construction Engineering, Oregon State University, Corvallis, OR 97331, *Corresponding Author*

ABSTRACT

This study presents the use of controlled blasting as a source of seismic energy to obtain the coupled, dynamic, linear-elastic to nonlinear-inelastic response of a plastic silt deposit. Characterization of blast-induced ground motions indicate that the shear strain and corresponding residual excess pore pressures (EPPs) are associated with low frequency near- and far-field shear waves that are within the range of earthquake frequencies, whereas the effect of high frequency P-waves are negligible. Three blasting programs were used to develop the initial and pre-strained relationships between shear strain, EPP, and nonlinear shear modulus degradation. The initial threshold shear strain to initiate soil nonlinearity and to trigger generation of residual EPP ranging from 0.002 to 0.003% and 0.008 to 0.012%, respectively, where the latter corresponded to ~30% of G_{max}. Following pre-straining and dissipation of EPPs within the silt deposit, the shear strain necessary to trigger residual excess pore pressure increased two-fold. Greater excess pore pressures were observed in-situ compared to that of intact direct simple shear (DSS) test specimens at a given shear strain amplitude. The reduction of in-situ undrained shear strength within the blast-induced EPP field measured using vane shear tests compared favorably with that of DSS test specimens.

INTRODUCTION

Geotechnical earthquake engineering practice regarding the seismic response of silt deposits generally center on assessments of their cyclic and post-cyclic responses. Such assessments may consider the plasticity index, *PI*, fines content, *FC*, overconsolidation ratio, *OCR*, effective confining or vertical stress, σ'_{v0}, static shear stress, and soil fabric (Sanin and Wijewickreme 2006; Soysa 2015; Dahl et al. 2010, 2014; Beyzaei et al. 2019; Wijewickreme et al. 2019; Jana and Stuedlein 2020). Critical dynamic soil properties useful for calibrating site response and constitutive models include the threshold shear strain to trigger nonlinearity, γ_{te}, threshold shear strain to trigger nonlinear-inelasticity and generate residual excess pore pressure, γ_{tp}, and the relationship between shear strain amplitude and residual excess pore pressure ratio, $r_{u,r}$, defined as ratio of residual excess pore pressure, $u_{e,r}$, and σ'_{v0} (e.g., Hashash et al. 2010; Markham et al. 2016). Quantification of constitutive threshold shear strains and relationships between shear strain, γ, and $r_{u,r}$ have been largely based on strain-controlled cyclic tests on reconstituted specimens (Hsu and Vucetic 2006; Mortezaie and Vucetic 2016) and a few studies performed on intact specimens (Tabata and Vucetic 2010; Ichii and Mikami 2018).

Best practices for the evaluation of the cyclic resistance of silt generally consist of conducting tests on relatively undisturbed soil samples (Boulanger et al 1998; Bray and Sancio 2006; Boulanger and Idriss 2007), where sample quality is evaluated using changes in void ratio during recompression (Lunne et al. 2006), recompression index ratio (DeJong et al. 2018), and shear wave velocity criteria. Some amount of disturbance is inevitable and is generally more severe for silts of lower plasticity, the consequence of which is significantly lower cyclic resistance relative to *in-situ* conditions (Kurtulus and Stokoe 2008; Dahl et al. 2010; Wijewickreme et al. 2019). Whereas significant progress has been made in understanding the elemental cyclic response of silt in the laboratory, researchers have identified differences between the observed *in-situ* penetration test-based (Cubrinovski 2019; Yost et al. 2019) and laboratory-predicted response of natural silts (Beyzaei et al. 2018, 2019). The complexity of the *in-situ* dynamic response arises from excess pore pressure diffusion, soil variability, interlayering, and multi-directional seismic shaking (Dobry and Abdoun 2015; Adamidis and Madabhushi 2018, Beyzaei et al. 2018, 2019; Ni et al. 2020; Jana and Stuedlein 2021), which are difficult to simulate in laboratory settings.

Evaluation of the *in-situ*, nonlinear-inelastic, coupled shear strain and excess pore pressure can serve to address the aforementioned needs in geotechnical earthquake engineering. One established and successful approach to capture the dynamic *in-situ* response of soils uses large mobile shakers with embedded sensor arrays and application of horizontal or vertical shaking to the ground surface or a deep foundation, respectively (Chang et al. 2007; Kurtulus and Stokoe 2008; Cox et al. 2009; Stokoe et al. 2014; Roberts et al. 2016, Zhang et al. 2019). The more common technique with horizontal shaking of the ground surface is appropriate for relatively shallow soils (e.g., 3 to 4 m; van Ballegooy et al. 2016) with a ground surface that can transmit the imposed energy to the instrumented layers. Gohl et al. (2001) demonstrated the utility of alternate sources of seismic energy, specifically the detonation of explosives, to provide an indication of the nonlinear-inelastic response of soils at greater depths; however, the understanding of the constitutive soil response to blast-induced ground motions and mechanisms of excess pore pressure generation remains limited.

Few studies present a direct comparison of the dynamic, coupled, *in-situ* and laboratory element responses. Kurtulus and Stokoe (2008) tested unsaturated non-plastic silty soils to determine their *in-situ* shear modulus reduction behavior, with shear strains generally limited to 0.05%, just larger than typical γ_{tp}. Excess pore pressures were not measured, likely due to the low degree of saturation of the soil. However, implementation of shear modulus, *G*, and reference shear strain scaling techniques demonstrated that the normalized laboratory element and *in-situ* responses were comparable over the small-to-medium range in strain investigated. In ideal conditions, a seismic energy source could be supplied to achieve small-to-large shear strains at any depth and the corresponding coupled behavior observed to deduce robust *in-situ* dynamic soil properties to identify similarities and differences with laboratory element test observations. Jana and Stuedlein (2021) present one such example for medium dense sands at an average depth of 25 m and with direct simple shear-equivalent shear strains exceeding 1%; however, similar observations for plastic soils at depth have not been reported.

This study presents the application of controlled blasting to obtain the coupled, dynamic properties of an alluvial plastic silt deposit from the linear-elastic to nonlinear-inelastic constitutive regimes. First, the characterization of the deposit based on subsurface and laboratory investigations performed *in-situ* and on specimens derived from undisturbed samples is presented. The experimental approach and controlled blasting program is described, followed by the characterization of blast-induced ground motions in terms of their body wave components and frequency content, and their influence on the soil response to demonstrate the appropriateness of the technique. The relationship between the *in-situ* shear strain, excess pore pressure generation, shear modulus degradation, and loss of strength in the silt deposit is then presented. The *in-situ* and laboratory-based dynamic responses is compared to identify similarities and differences in their behavior and establish the benefit of *in-situ* testing using the controlled blasting technique.

EXPERIMENTAL SETTING AND SOIL CHARACTERIZATION

Site and Subsurface Conditions

The experiments were conducted at a test site located at the Port of Portland, Portland, OR, approximately 1 km southeast of and aligned with the South Runway at Portland International Airport. Figure 1a illustrates the relevant components of the experiments, including blast casings, pore pressure transducers (PPTs), velocity transducers, and the locations of explorations. The linear experimental array of blast casings and instruments extends approximately 45 m in length and focuses on two separate instrumented arrays, termed the Sand Array (25 m center depth; Jana and Studlein 2021) and the Silt Array (10.2 m center depth), the latter of which forms the basis for this study. Subsurface investigations included thin-walled tube sampling, cone penetration tests (CPTs) with dissipation, vane shear tests (VSTs), and downhole geophysical tests. Dredge sand and silty sand fill comprise the upper 5 to 6 m of the subsurface, and is underlain by an approximately 2 m thick layer of native, alluvial, loose, clean sand. Below the native sand deposit lies the 5 to 6 m thick alluvial, medium stiff, plastic silt (ML and MH) deposit with traces of sand and thin stringers of sandy silt (ML). Extending below and to the 30 m depth of the explorations lies a deposit of alluvial, medium dense, clean sand (SP) to sand with silt (SP-SM; Jana and Stuedlein 2021). The groundwater table depth varied from 3.0 to 7.3 m associated with seasonal fluctuations in the Columbia River and occasional dewatering operations conducted at and adjacent to nearby Port facilities.

Geotechnical Characterization of the Plastic Silt Deposit

Installation of instruments necessary to conduct the experiments were preceded by thin-walled tube sampling using an Osterberg piston sampler within mud-rotary boreholes B-4 and B-6 (Fig. 1a). The average and range in corrected cone tip resistance, q_t, and Soil Behavior Type Index, I_c (Robertson 2009) is 0.97 MPa and 0.82 to 1.19 MPa, and 3.0 and 2.9 to 3.1, respectively, from depths of 8.9 to 11.7 m corresponding to the Silt Array and thin-walled tube samples (Fig. 1b).

The *PI* of the silt deposit varied from 14 to 39 with an average of 28 (Fig. 1c), whereas the *OCR* varied from 1.6 to 2.2 (Fig. 1f). The average compressive wave velocity, V_p of intact specimens consolidated to $\sigma'_{vc} = \sigma'_{v0}$ determined using bender disk tests was 1,030 m/s compared to an average of 940 m/s from downhole and crosshole geophysical testing (Fig. 1e). The average shear wave velocity, V_s, of specimens consolidated to their *in-situ* stresses was approximately 122 m/s, similar to that obtained using geophysical tests (Fig. 1d). Vane shear tests were conducted prior to and immediately following the Shallow Blast Program indicated an initial, average undrained shear strength ratio, $s_{u, VST}/\sigma'_{vc}$ of 0.56, slightly larger than the monotonic, direct simple shear (DSS) test-based $s_{u, DSS}/\sigma'_{vc} = 0.49$ (Fig. 1g). Undrained shear strengths correlated to q_t agreed with the DSS and vane shear strengths. Constant-volume, cyclic, stress- and strain-controlled DSS tests were conducted on intact silt specimens (Jana and Stuedlein 2020) for comparison of the *in-situ* and laboratory-based responses of the silt and presented below. Comprehensive details are in Jana and Stuedlein (2020).

EXPERIMENTAL PROGRAM

Instrumentation Comprising the Silt Array

Instruments necessary to capture the *in-situ* response to controlled blasting were installed within 200 mm mud-rotary boreholes and grouted to form the Shallow Array (Fig. 2). The geometry of the Silt Array allowed quantification of the shear modulus, G, and u_e with the shear strains imposed, where shear strain is deduced from displacement-based finite element analysis (FEA) framework proposed by Rathje et al. (2005) and implemented in various studies (Chang et al. 2007; Cox et al. 2009; Stokoe et al. 2014; Roberts et al. 2016, 2017; Cappa et al. 2017; Zhang et al. 2019; Jana and Stuedlein 2021). Shown in Figs. 1 and 2, the Silt Array consisted of four boreholes: (1) I-2 housed a full-depth inclinometer casing fitted with sondex settlement rings to capture post-shaking volumetric strains (Fig. 1a, I-2), (2) B-5 drilled to place the pore pressure transducer (PPT) string, and (3) B-4 and B-6 drilled to place the triaxial geophone packages (TGPs), which consisted of 28 Hz triaxial geophones and a six-axis accelerometer gyroscope to capture static tilt. The TGPs were placed to form two rectangular finite elements with nodal displacements derived from the recorded particle velocities. The location of the PPTs were selected to represent the center of each element and correspond to the location of shear strain computation. The effort to calibrate, locate, and orient each instrument is described in detail by Jana et al. (2021).

Summary of Blast Programs Conducted

In-situ dynamic testing was performed using three separate controlled blasting events: (1) the Test Blast Program (TBP) (2) the Deep Blast Program (DBP) and (3) the Shallow Blast Program (SBP). These blast events were performed on three consecutive days starting on 3 October 2018. The TBP was performed in order to obtain the small-strain linear-elastic baseline crosshole response of the soil, assess the functionality of the various sensors and data acquisition systems, and evaluate attenuation relationships. The primary objective of the DBP was to excite the Sand Array (Fig. 1a, Jana and Stuedlein 2021), whereas the SBP was primarily executed to excite Silt Array. Seismic energy produced during each blast program was registered in the Silt Array and are used to interpret the responses, and changes in constitutive response, described herein.

The controlled blasting programs used Ikon electronic detonators, Cordtex detonation cord, and Pentex cast boosters with an explosive detonation pressure and velocity of 24 MPa and 7,900 m/s respectively. The TBP implemented eight charges varying from 0.227 to 3.628 kg set within a single blast casing CX located approximately 30 m west from blast casing C1 (Fig. 1a) that extended to a depth of 27.4 m. The DBP and the SBP each consisted of thirty charges spatially-distributed within the blast casings C1 to C10 and C6 to C15, respectively (summarized in Table

1). Figure 3 illustrates the 30s detonation time history and corresponding charge locations for the SBP, indicating a progressive increase in charge weight to Blast #13 and #14, upon which the charge weight progressively reduced as the distance between successive charges and the Silt Array decreased. The detonation of successive charges alternated between the west and east sides of the Silt Array in order to alternate the polarity of the seismic signal (Heelan 1953), and to roughly approximate unbiased cyclic loading of the Silt Array.

Computation of Shear Strain

The general approach used to compute the imposed shear strains followed the displacement-based FEA described by Cox et al. (2009). The selected approach does not require the assumption of plane wave propagation and is appropriate for shear strain estimation in any seismic wavefield (Cox 2006); this approach has been widely-implemented for *in-situ*, large scale, and centrifuge tests to evaluate dynamic shear strains (e.g., Chang et al. 2007; Stokoe et al. 2014; Roberts et al. 2016; Cappa et al. 2017; Zhang et al. 2019; Jana and Stuedlein 2021). Two isoparametric finite elements were formed by the Silt Array where TGPs S3, S4, S7, and S6 form the nodes of Element 1 and TGPs S4, S5, S8, and S7 form the nodes of Element 2 (Fig. 2). Measured particle velocities in each TGP are corrected to the east-west or longitudinal, x, and vertical, z-direction using the true bearings of the mutually-perpendicular geophone axes as described by Jana et al. (2021). Particle velocities, V_x and V_z, were integrated to obtain the particle displacements, D_x and D_z, at each node. Thereafter, the Cauchy shear strains (i.e., normal strains ε_{xx}, ε_{zz} and shear strain, γ_{xz}) in each element were computed from D_x and D_z using appropriate shape functions (e.g., Chandrupatla et al. 2002). The full waveform including compression or P-waves, the near-field shear or S-waves, and the far-field S-waves were used to compute the shear strain in the soil, thus allowing decomposition of the influence of each body wave component in the dynamic soil response. Owing to the dimensionality of each blast pulse (addressed below), the octahedral shear strain, γ_{oct} induced in the soil is computed from the Cauchy strain tensor assuming plane strain conditions for comparison to DSS test results using (Cappa et al. 2017):

$$\boldsymbol{\gamma_{oct}} = \left(\frac{2}{3}\right)\sqrt{(\boldsymbol{\varepsilon_{xx}})^2 + (-\boldsymbol{\varepsilon_{zz}})^2 + (\boldsymbol{\varepsilon_{zz}} - \boldsymbol{\varepsilon_{xx}})^2 + \mathbf{6}\left(\frac{\gamma_{xz}}{\mathbf{2}}\right)^{\mathbf{2}}} \qquad \mathbf{(1)}$$

where all variables have been previously defined.

CHARACTERIZATION OF BLAST-INDUCED GROUND MOTIONS

Ground motions associated with controlled blasting differ from the commonly-assumed vertically-propagating horizontally-polarized shear waves associated with earthquakes (Seed 1979): indeed, the former depends on both the source-to-site distance (i.e., observation distance) and the scale of interest (Heelan 1953; Blair 2010, 2015; Gao et al. 2019). Buried explosives produce a very short duration, high-pressure compressive shock wave (*P*-wave) that propagates radially from the source through the soil (Dowding and Duplaine 2004), followed by vertically-polarized shear or SV-waves generated upon unloading of the expanding shockwave front (Hryciw 1986; Fragaszy and Voss 1986; Narin van Court and Mitchell 1994; Gianella and Stuedlein 2017). Although the peak amplitude of the *P*-wave particle velocity from controlled blasting can be quite large, particularly in comparison to earthquake loading as observed near the surface and away from the fault rupture plane, it has been shown for saturated sands (Jana and Stuedlein 2021) that the associated predominant frequency is so high as to prevent significant displacements, shear strain, and residual excess pore pressures, $u_{e,r}$, in soil as postulated by Ishihara (1967).

Dynamic Soil Response to P- and S-waves

Figure 4 presents the measured velocities, integrated displacements, and corresponding soil responses associated with 90 and 150 g charges detonated at a large and small distance, respectively, from the Silt Array as observed during the SBP. The longitudinal and vertical components of the measured ground motions V_x and V_z, and corresponding D_x and D_z, normalized to their maximum amplitudes are shown in Figs. 4a and 4b for SBP Blast #1 recorded in TGP S3. Particle velocity records indicate that the relatively high-frequency longitudinal *P*-wave (with f_{P_X} = 80 Hz) is followed by a lower-frequency ($f_{near\text{-}field,SV_X}$= 40 Hz) near-field SV_X-wave generated due to the three-dimensional seismic disturbance (Fig. 4a; Sanchez-Salinero et al. 1986). Following the *P*-wave arrival (i.e., 0.1 s), a low-frequency ($f_{far\text{-}field,SV_Z}$= 21 Hz) far-field SV_Z-wave was registered by TGP S3z (Fig. 4b). The maximum V_x and V_z measured during SBP Blast #1 were 0.0077 and 0.0063 m/s, respectively, corresponding to maximum D_x and D_z of 0.057 and 0.051 mm which occurred in response to the low-frequency far-field SV-wave generated at the charge location. Figure 4c illustrates the measured u_e response and corresponding increment in γ_{oct} derived using displacement-based FEA. The maximum octahedral shear strain, $\gamma_{oct,max}$ during SBP Blast #1 was 0.011% in Element 1. Although passage of the *P-wave* produced a maximum excess pore pressure ratio, $r_{u,pmax}$ = 5.88%, its high frequency prevented significant shear strain upon unloading, limiting it to approximately 25% of $\gamma_{oct,max}$ and resulting in a nonlinear-elastic soil response preventing generation of $u_{e,r}$ (Ishihara 1967). The shear strain magnitude was smaller than the threshold shear strain to trigger residual excess pore pressures as observed by Hsu and Vucetic (2006) and Mortezaie and Vucetic (2016). Note that the *SV* waves generated by the unloading of the *P*-wave was responsible for $\gamma_{oct,max}$ owing to their low-frequency content.

Figures 4d and 4e illustrate the normalized particle velocities and displacements in TGP S3 during SBP Blast #30 (150 g charge) corresponding to a small source-to-site distance. In this case, the near- and far-field *SV*-waves are superimposed upon one another as described by Sanchez-Salinero et al. (1986) due to the small space-time provided to the far-field *SV*-wave to traverse the Silt Array. Due to small distance and limited filtering and attenuation provided, the predominant frequency of the *P-wave* was 180 and 350 Hz in the longitudinal and vertical directions, respectively, whereas the frequency of the near- and far-field *SV* waves was 32 and 22 Hz, respectively. The high-frequency *P*-wave limited *P*-wave induced displacements to 5 and 19% of the maximum D in the x and z directions, respectively; D_{max} was again associated with the low-frequency superimposed *SV*-waves. Figure 4f illustrates the measured u_e and corresponding increment in γ_{oct} calculated for Element 1 and SBP Blast #30. The $\gamma_{oct,max}$ in the silt was 0.267% with an incremental γ_{oct}, $\Delta\gamma_{oct}$, equal to 0.066%. Although the *P*-wave produced $r_{u,pmax}$ = 181.6%, the elastic nature of the *P*-wave (Ishihara 1967) could not produce residual excess pore pressure; rather, passage of the near- and far-field *SV*-waves provided sufficient γ_{oct} to produce $r_{u,r}$ = 12.3%. Inspection of Fig. 4f and the inset figure indicates direct correlation of time and frequency between the shear strain and shear-induced r_u. The shear strain and corresponding residual excess pore pressures developed during controlled blasting are associated with the low-frequency shear waves as suggested by Gohl et al. (2001), despite existing correlations to one-dimensional compressive strain amplitudes (e.g., Charlie 1992, 2013).

Figures 5a to 5c illustrates the full particle velocity time histories recorded using TGP S7 during the 8 s TBP, 30 s DBP, and 30 s SBP. The magnitude of the particle velocity is governed by the ray path distance between the charge location and the TGP and the charge weight. Since charges detonated during the TBP were located far away (i.e., 63 m) from the Silt Array (Fig. 1a), the maximum particle velocities were significantly lower than those measured during the DBP and SBP. The constitutive soil response ranged from linear–elastic, to nonlinear-elastic, to nonlinear-inelastic over the course of the three blast programs as described in detail below.

Frequency Content of Blast-induced Ground Motions

The frequency content of the various body wave components associated with controlled blasting may be conveniently identified using the short-term Fourier transformation termed the normalized Stockwell spectrogram (Stockwell et al. 1996), indicating the evolution of body wave frequency with time (Kramer et al. 2016). Figure 6a illustrates the variation of the frequency-time response of the *P*-, near-, and far-field *SV*-waves for TGP S3x during SBP Blast #10, whereas the corresponding Fourier amplitude spectra of the same record is presented in Fig. 6b with a predominant frequency, *f*, of 13 Hz. Figure 6c presents the predominant *f* associated with the relevant components of the *P*- and *SV*-waves during the SBP for TGP S3 and S5. The predominant frequencies for the *P*-waves range from 75 to 800 Hz and increased as the distance between the source and site decreased, owing to decreased attenuation and filtering of the high-frequency energy. The frequency of near-field *SV* waves varied from 9 to 45 Hz with an average $f = 27$ Hz, whereas *f* for the far-field *SV* waves ranged from 10 to 33 Hz, with an average $f = 17$ Hz. The predominant *f* of the *SV* waves decreased as blasting proceeded in response to the dynamic softening of the silt due to increased shear strain and the generation of $u_{e,r}$. The predominant frequency of the far-field *SV*-waves decreased initially, and then increased, and again decreased in response to changes in the rate of drainage during the SBP as described below. In general, the blast-induced *SV*-wave frequencies are within the range of the earthquake ground motions and were responsible for the maximum seismic strain energy responsible for the global dynamic silt response, despite the amplitude of the blast-induced *P*-waves.

Dimensionality of Body Waves

Body wave fronts and associated blast-induced ground motions may be considered 2D plane waves or 3D waves depending on the source–to-observation distance and the scale of the observation (i.e., size of the array; Heelan 1953; Sanchez-Salinero et al. 1986; Blair 2015; Gao et al. 2018). Seismic waves recorded at a significant distance from the energy source and presented here could often be assumed as 2D plane waves. For example, the vertical particle velocity records of two vertically-adjacent geophones within the same borehole exhibited similar amplitudes and phase differences of the propagating *SV*-waves during many blasts (i.e., Figs. 5d to 5k) to indicate a 2D planar shear wave field traversing the Silt Array. Subtle differences in the particle velocities represent local variation in soil properties, ray path distances, and the local diameter of the grout column encapsulating the TGPs. Variability within the natural silt deposit was identified during the subsurface and laboratory investigation (Figs. 1b to 1g). Ground motions associated with the detonation of a charge close to the Silt Array are shown in Figure 5l (SBP Blast #30), illustrating a significant phase difference between the two-particle velocity records within the same borehole, indicative of a 3D wave field. Use of the displacement-based FEA to compute shear strain does not require 1D wave approximations used by Charlie et al. (2013) and are appropriate for any seismic wave field (Cox et al. 2009).

IN-SITU DYNAMIC RESPONSE OF THE PLASTIC SILT DEPOSIT

Generation of Excess Pore Pressure with Shear Strain

The response of the Silt Array observed during the 8 s Test Blast Program (TBP) was described by Jana et al. (2021) to illustrate the feasibility of the dynamic test method used in this study. The maximum γ_{xz} observed during the TBP was 0.0118% and 0.0072% for Elements 1 and 2, respectively, and the maximum residual γ_{xz} was 0.0073% and 0.0033%. TBP Blast #8 produced $r_{u.r}$ = 0.35%, and 0.77% at Elements 1 (PPT-2) and 2 (PPT-3) respectively, indicating exceedance of the threshold shear strain, γ_{tp} to trigger residual excess pore pressure in the silt.

Table 2 summarizes results for the TBP reported by Jana et al. (2021) and compares γ_{tp} and $r_{u.r}$ for the TBP and SBP.

The charges detonated during the Deep Blast Program (Table 1) were primarily used to excite the Sand Array as described by Jana and Stuedlein (2021); however, the energy produced during the DBP excited the Silt Array and the measured body waves have been used to further establish the shear strain-dependent trends in excess pore pressure generation in the Silt Array. The particle velocities recorded in TGP S7 are shown in Fig. 5b for the entire blast program, whereas Figs. 5e, 5h, and 5k present the full waveform of the vertical particle motion for TGP S7z and S8z. Figs. 7a- 7c present the γ_{xz}, γ_{oct}, and r_u time histories in the Silt Array resulting from the DBP. Due to the proximity of the second charge (i.e., DBP Blast #2) to the Silt Array (approximately 5 m; Fig. 1a and Table 1), the particle velocity is significantly greater than similar charges (i.e., 90 g charges, DBP Blasts #1, #3, and #4). For example, the peak body wave velocity measured in TGPs S3 and S7 for Blast #2 was 20- and 5-fold larger than Blasts #1 and #3, resulting in a maximum γ_{xz} for Blast #2 that was approximately 40 times larger than that of Blasts #1 and #3. Blast #1 produced γ_{xz} equal to approximately 0.0018%, which was insufficient to trigger $u_{e,r}$, whereas Blast #2 exhibited significant $u_{e,r}$ (Fig. 7c). Figures 7a – 7c show that as blasting continued and detonated charges approached the center of the Sand Array, the dynamic loading of the Silt Array reduced. The absolute maximum γ_{xz} induced by Blast #2 was equal to 0.0525 and 0.0666% for Elements 1 and 2, respectively (Fig 7b) and the threshold shear strain to trigger $r_{u,r}$ was exceeded, considering $r_{u,r}$ equal to 1.97% and 6.01% in Elements 1 and 2, respectively, following Blast #2. Due to the proximity of Element 2 to Blast #2, a significant positive residual shear strain developed, and slowly reversed in direction as the ray path orientation changed over the course of the detonation time history. On the other hand, Element 1 exhibited a gradual increase in accumulated shear strain with time. The maximum absolute γ_{xz} in Elements 1 and 2 were equal to 0.1230% and 0.1155%, respectively, with a maximum residual γ_{xz} of 0.0853% and 0.0729%, respectively. The maximum γ_{oct} in Elements 1 and 2 were equal to 0.1472% and 0.1917%, respectively, with corresponding $r_{u,r}$ equal to 5.39% and 5.69% in Elements 1 and 2, respectively. Following detonation of the DBP, $r_{u,r}$ slowly increased in response to the significant $r_{u,r}$ generated in the sand layer directly below it (Jana and Stuedlein 2021), indicative of upward water flow (Cubrinovski et al. 2019).

The Shallow Blast Program (Table 1, Fig. 3) was conducted primarily to excite the Silt Array and produced the largest amplitudes of dynamic loading to the silt layer (with maximum V = 0.28 m/s; Fig. 5c). Figure 8 presents examples of blast-induced shear strain waveforms and corresponding r_u in Elements 1 and 2, indicating the accumulation of γ_{xz} and $r_{u,r}$ during the SBP and that the variation in r_u is correlated to the shear strain in time and amplitude. Figures 7d- 7f present the γ_{xz}, γ_{oct}, and r_u time histories in the Silt Array during the SBP. The maximum γ_{xz} induced within Elements 1 and 2 was 0.27% and 0.13%, respectively, and resulted in a peak in-shear r_u = 22% and 17% in Elements 1 and 2, respectively. Following the SBP, the residual γ_{xz} in Elements 1 and 2 was equal to 0.19% and 0.056%, respectively. The larger peak and residual shear strains within Element 1 resulted in the largest $r_{u,r}$ = 12.6% as compared to Element 2 ($r_{u,r}$ = 8.2%).

The TBP resulted in relatively small γ_{oct} within Element 2 but produced the largest excess pore pressure (exceeding γ_{tp}) corresponding to the smallest residual shear strain (Jana et al. 2021). On the other hand, Element 2 produced the largest u_e and residual γ_{oct} during the DBP (Figs. 7b and 7c), due to the proximity of Blast #2 and the role of charge length on the shear wave amplitude and ray path (Blair 2010). However, it is noted that following DBP Blast #2, the excess pore pressure in Element 1 responded more strongly to continued blasting (Fig. 7c). This suggests that the consistency and plasticity in Elements 1 and 2 are somewhat different from one another (Fig

1c) and that the unsampled soil between 10.47 and 11.13 m may have exhibited lower *PI* than determined from tests on sampled soils (Fig.1c). This observation appears to be confirmed in Fig. 7e, where Element 2 produced the smallest γ_{oct} and exhibited drainage during the latter half of the SBP (Fig. 7f). Occasional lenses of sandy silt revealed in the CPT data and laboratory test analyses (e.g., at 8.71 m depth: FC = 74% and PI = 14) could provide drainage pathways for the overall silt deposit (with FC > 95%, PI > 25).

In Situ Relationship between Shear Strain and Excess Pore Pressure

To compare the maximum mobilized *in-situ* shear strain during the three blast programs with the DSS tests conducted on intact specimens reported by Jana and Stuedlein (2020), the DSS-equivalent, constant-volume shear strain, $\gamma_{DSS,eq}$ was computed using γ_{oct} by imposing constant volume boundary conditions on Eq. 1 (Cappa et al. 2017):

$$\boldsymbol{\gamma_{DSS,eq} = \sqrt{\frac{3}{2}}\gamma_{oct}} \qquad \textbf{(2)}$$

The three blast events described above were used to construct the relationship between the maximum DSS-equivalent shear strain, $\gamma_{DSS,max}$, for each blast-induced waveform and the maximum shear-induced excess pore pressure ratio, $r_{u,max}$, and $r_{u,r}$. Two additional finite elements derived from the Silt Array were formulated to evaluate the effect of element shape on the dynamic response to the SBP and enable the use of PPT 5 (Fig. 2). Elements 3 and 4 were constructed as rhombus-shaped elements consisting of TGPs S8, S4, S3, and S7, and TGPs S7, S5, S4, and S6, respectively. The maximum shear strain, $\gamma_{DSS,max}$ imposed during the three blast events was 0.35% (Element 1), resulting in a corresponding $r_{u,max}$ = 24%. The largest in-shear $r_{u,max}$ observed was 31% which occurred during the DBP in Element 2 in response to a peak shear strain ($\gamma_{DSS,max}$) of 0.20%. Note that the γ - r_u relationship presented in Fig. 9a does not indicate how the number velocity pulses (i.e., "cycles") relate to u_e, as commonly interpreted using equivalent uniform cycles, N, and the resulting scatter is apparent in Fig. 9a.

Figure 9b presents the variation of maximum $r_{u,r}$ with $\gamma_{DSS,max}$, representing a standard presentation of strain-controlled cyclic DSS test data (e.g., Hsu and Vucetic 2006; Mortezaie and Vucetic 2016). Although some scatter remains, the variability in the overall shear strain-pore pressure response is significantly smaller than that presented in Fig. 9a. The threshold shear strain to trigger excess pore pressure is apparent, and excess pore pressure rises rapidly for $\gamma_{DSS,max} > \gamma_{tp}$ = ~0.01%, consistent with previously-reported cyclic data on plastic soils (e.g., Mortezaie and Vucetic 2016). The largest $r_{u,r}$ observed was approximately 15% and corresponded to $\gamma_{DSS,max}$ = 0.20 to 0.35%. The maximum shear-induced $r_{u,r}$ was equal to 15%, 12.6%, and 8.8% as observed in the middle of the Silt Array (PPT 5, Elements 3 and 4), Element 1, and Element 2, respectively. Greater excess pore pressures developed in Element 1 compared to Element 2, attributed to variability in the silt deposit within the instrumented array as described above. Considering that the average *PI* for Elements 1 and 2 was 27 and 29, the average *OCR* derived from oedometric testing for Elements 1 and 2 was 1.86 and 2.1 (Jana and Stuedlein 2020), and the average $s_{u,VST}/\sigma'_{vc}$ for Elements 1 and 2 was 0.59 and 0.67, respectively, the greater stiffness of Element 2 served to prevent larger shear strains and corresponding excess pore pressures.

Table 2 presents γ_{tp} for the *in-situ* finite elements observed during the three blasting events (note that γ_{tp} could not be clearly defined for the DBP due to Blast #2). However, the dissipation of the relatively large residual excess pore pressure (i.e., $r_{u,r}$ = 5%) in the DBP resulted in two-fold increase in γ_{tp} relative to the initial γ_{tp} observed during the TBP (i.e., 0.008 to 0.0016%; Table 2). This observation is consistent with the measured increase in V_s within the Silt Array following the

DBP, discussed further below. Silt subjected to low amplitude shear strains results in an increase in its dynamic shearing resistance (Soysa and Wijewickreme 2019).

Comparison to Laboratory Test-based Excess Pore Pressure-Shear Strain Relationships

Constant-volume, strain-controlled cyclic DSS tests were performed on intact specimens prepared from thin-walled tube samples to develop the cyclic excess pore pressure versus cyclic shear strain relationship (Jana and Stuedlein 2020). Specimens were consolidated to the *in-situ* $\sigma'_{vc} = \sigma'_{v0} = 106$ kPa and cyclically-sheared with various amplitudes of uniform shear strain cycles at $f = 0.1$ Hz. Development of u_e during cyclic shearing was inferred from the reduction in σ'_v under constant volume per Dyvik et al. (1987). Figure 9c presents the comparison of $r_{u,r}$ with $\gamma_{DSS,max}$ for the *in-situ* and DSS test results: the range in γ_{tp} of 0.008 to 0.012% measured *in-situ* is similar to that obtained in the laboratory, however, the *in-situ* tests produced greater u_e than that measured in the laboratory for $\gamma_{DSS,max} > 0.01\%$. This observation is somewhat surprising, given that the laboratory tests are conducted under an artificially-imposed undrained (i.e., constant-volume) boundary condition, whereas the excess pore pressures in the field are allowed to drain during shaking. The initial slope of the $\gamma_{DSS,max}$-$r_{u,r}$ curve (i.e., in proximity to γ_{tp}) derived from the *in-situ* test results does not suffer from apparatus compliance and is representative of a larger soil volume; therefore, the *in-situ* test results presented herein are considered more reliable for representing the global response of the plastic silt deposit.

Shear Modulus Degradation with Shear Strain

Extensive downhole and crosshole testing provided the baseline and post-event maximum shear modulus, G_{max}, for normalization of G. Although some degree of anisotropy in V_s determined using the vertically-propagating horizontal shear (SH) waves and horizontally-propagating SV-waves was expected, no significant anisotropy was observed in the Silt Array (Donaldson 2019). Thus, downhole measurements made following each blast event and computed using the interval method (ASTM 2019) could be used for development of G/G_{max} curves. Apparent consolidation of the silt deposit followed the DBP and resulted in an apparent increase in V_s. Table 3 presents the average downhole small-strain (i.e., linear-elastic) V_s for various TGP pairs measured in the Silt Array before the TBP and SBP, which ranged from 119 to 154 m/s for any given TGP pair, indicative of the variability observed within CPT-3. A representative V_s = of 126 m/s appears appropriate for the initial, pre-TBP conditions and was confirmed using the small strain crosshole V_s observed during the TBP.

The strain-dependent shear wave velocity was calculated for each of the laterally-offset TGP pairs using the crosshole time delay of the far-field *SV*-waves and the corresponding ray path distances. Since the elevation of the charges and TGP pairs were not necessarily shared (compare Fig. 2 and Table 1), the direct linear ray path from the center of the charge to the TGP was used to compute V_s (Heelan 1953). Figure 10a illustrates the three orthogonal components of an example particle velocity record (TBP Blast #3) demarcating the arrival of various body waves. The approximate time of arrival of the far-field *SV*-wave was estimated using the crosshole V_p, initial or antecedent crosshole V_s, and the direct linear ray path distance. The computed arrival time is somewhat later than the actual arrival time, possibly due to: (a) placement of the charge at the interface of the silt and underlying sand layer, the latter of which exhibits a higher V_s; (b) possible variation in the depth to the interface of these layers between the charge and the array, and (c) possible variation in *Vs* in the materials between the charge and the array. Arrival times of the far-field shear wave were verified using the normalized Stockwell spectrogram of the longitudinal (TGP S3x) and transverse (TGP S3z) particle velocities, the former of which is shown in Fig. 10b and indicated a reduction in the predominant frequency of the far-field *SV*-wave following passage of and relative to the near-field *SV*-wave. The time delay between the *SV*-waves recorded in laterally-offset TGPs within different boreholes are shown in Fig. 10c and 10d; this time delay and the difference in the ray path distances were used to calculate the crosshole V_s within the Silt Array. Note that the arrival of the shear wave and the shear wave velocity changes throughout the blast programs due to the strain-dependent nonlinearity of the soil.

The strain-dependent crosshole V_s resulting from each blast in the Test and Shallow Blast Programs, and corresponding shear modulus reduction, is presented in Fig. 11 in terms of $\gamma_{DSS,max}$. Figure 11a demonstrates that: (1) the linear-elastic regime was maintained through $\gamma_{DSS,max}$. ≈ 0.002 to 0.003%, based on the lack of scatter in V_s in this range of shear strain, and (2) the linear-elastic threshold shear strain, γ_{te}, was exceeded to demonstrate observable nonlinearity during the relatively small excitation of the TBP (Table 1; Jana et al. 2021). The crosshole *Vs* corresponding to the linear-elastic shear strain was used as the basis for normalization of *G* for data derived from the TBP. As the TBP continued, the soil responded nonlinearly and with a degradation in its wave transmissibility (by about 15%) at the end of the TBP. The maximum residual excess pore pressure ratio generated in the Silt Array following the TBP was 0.77%, and little change in soil fabric was anticipated as a result of the TBP based on laboratory cyclic test data on plastic soils reported by Hsu and Vucetic (2006).

Given the significantly different elevations between the charges in the DBP and the TGPs comprising the Silt Array, the ray paths were much steeper than those intended for crosshole testing and the number and reliability of ray paths crossing two TGPs for computation of a diagonal velocity was low (Sanchez-Salinero et al. 1986). Furthermore, liquefaction of the sand layer (Jana and Studlein 2021) in proximity to the charge and refraction following the passage through the silt/sand layer contact would have likely altered the ray path. Accordingly, the crosshole shear wave velocities corresponding to the DBP were not computed within the Silt Array. Downhole tests conducted following the DBP were performed to assess possible changes in the soil fabric as a result of the DBP, which generated a maximum $r_{u,r}$ = 5.69%. Table 3 indicates an average increase in V_s of 6%, associated with the dissipation of u_e generated during the DBP and corresponding consolidation (i.e., densification). Owing to the lack of body wave anisotropy noted by Donaldson (2019), the post-DBP (pre-SBP) downhole V_s was used as the basis of normalization of G for crosshole V_s measured during the SBP. Figure 11b presents the V_s-$\gamma_{DSS,max}$ data corresponding to the SBP along with the small-strain pre-SBP downhole V_s, and indicates a reduction in V_s of approximately 50% over the duration of the 30 s blast event. Element 1 experienced the largest shear strains and residual excess pore pressures (Figs. 7d – 7f) and therefore exhibited the greatest reduction in V_s

Determination of the Shear Modulus Reduction Curves for the Shallow Silt Array

The variation of the strain-dependent V_s during the TBP and SBP (Figs. 11a and 11b) was used to compute the reduction in shear modulus during the blast programs using:

$$\boldsymbol{G = \rho V_s^2} \tag{3}$$

where ρ is the density of the silt, estimated from representative laboratory test specimens and equal to 1,580 kg/m^3. The G_{max} for Elements 1 and 2 were equal to 23 and 25 MPa, and 29 and 28 MPa, for the TBP and SBP, respectively, and were used to normalize G for each G-$\gamma_{DSS,max}$ pair in Figure 11c. The shear modulus reduced to approximately 0.71 to 0.74G_{max} at $\gamma_{DSS,max} \approx \gamma_{tp}$ for the TBP and representing the initial soil fabric of the plastic silt deposit to provide a critical observation for calibration of constitutive models. The range in G/G_{max} reduced for the range in γ_{tp} deduced for the SBP as indicated in Figure 11c. Residual excess pore pressure ratios of 10 to 15% correspond to

0.25 to $0.50G_{max}$. The upperbound of 0.5 G_{max} appears to result from partial drainage and the corresponding higher stiffness of the silt layer at Element 2, as described above. Further, G reduced to the range of 0.25 to $0.35G_{max}$ for shear strains of about 0.23%. Note that $\gamma_{DSS,max}$ computed from observations of the SBP was 0.27% for Blast #28; however, the corresponding shear wave velocity for this blast exhibited a 3*D* wave-field and was not considered reliable, and was therefore excluded from Fig. 11c. Elements 1 and 2 exhibited drainage during the latter half of the SBP (Fig. 7f), and serves to explain the higher G observed for larger shear strains (Figure 11c). This observation is corroborated by the recent centrifuge studies on reconstituted sand reported by Adamidis and Madabhushi (2018) and Ni et al. (2020), as well as the observations of the Sand Array reported by Jana and Stuedlein (2021). Since drainage is unavoidable during earthquakes (Beyzaei et al. 2018, 2019) and owing to the frequency content of the ground motions, the *in-situ* tests reported herein produce realistic soil responses to seismic shaking.

Comparison to Laboratory Test-based G/G_{max} Relationships

The strain-controlled, constant–volume, cyclic DSS test results reported by Jana and Stuedlein (2020) allow the estimation of the secant shear modulus reduction with shear strain for comparison to the *in-situ* test results. Bender elements fitted to the DSS loading platens provided the small-strain shear modulus used to normalize G/G_{max} of the intact specimens consolidated to $\sigma'_{vc} = \sigma'_{v0}$ = 106 kPa. The secant shear modulus of each specimen was calculated using the first cycle of the shear stress-shear strain response for unique specimens subjected to a uniform shear strain amplitude. Figure 11c indicates that G degraded to 0.70 G_{max} at a shear strain of 0.01%, similar to the *in-situ* test results and approximately $0.2G_{max}$ at 0.1%, softer than that of the *in-situ* test results. Although good agreement between the DSS and *in-situ* G/G_{max} data is obtained in the nonlinear-elastic regime ($\gamma_{DSS,max}$ < 0.01%), the differences observed for larger shear strains stems from the increasing role of strain rate-effects associated with the use of a 0.1 Hz loading frequency in the DSS tests and to a lesser degree, apparatus compliance. Due to the difference in the frequency content of the blast-induced far-field *SV* waves (Fig. 6c) with the DSS testing (f =0.1 Hz), strain rate corrections were applied to the *in-situ* and laboratory G/G_{max} following the methodology proposed by Vardenga and Bolton (2013). The G/G_{max} data presented in Fig. 11d were corrected for the common earthquake frequency of 1 Hz, considering the strain rate of 0.01/s and assuming a strain rate-effect of 5% per $\log_{10}$ cycle (Vucetic and Tabata 2003; Vardenga and Bolton 2011, 2013).

Figure 11d also plots the shear modulus reduction curve interpolated from the Vucetic and Dobry (1991) family of G/G_{max} curves for plastic soils for representative *PI* of 25. The Vucetic and Dobry (1991) curves were based on data that exhibited significant scatter, larger than the scatter associated with measurements of *PI* obtained in the present study. Nonetheless, the Vucetic and Dobry (1991) G/G_{max} curves appear to capture the general trend of the *in-situ* G/G_{max}-$\gamma_{DSS,max}$ observations. Comparison of the *in-situ* test data to the Darendeli (2001) G/G_{max} curve for $PI = 30$ also indicates good agreement; though it is noted that the G/G_{max} curve for $PI = 30$ is lower than $PI = 25$ curve interpolated from Vucetic and Dobry (1991) and greater than the $PI = 28$ curve derived by Vardanega and Bolton (2013). Although the variation of G/G_{max} of these various curves varies from one another and were developed based on the limited, existing data, they generally follow the shear modulus degradation observed from the *in-situ* dynamic tests. Moreover, natural variability (Beyzaei et al. 2018), *in-situ* pore pressure migration (Adamidis and Madabhushi 2018) and strain rate-effects (Vucetic and Tabata 2003; Vardanega and Bolton 2011, 2013) present complications that may need to considered when predicting the *in-situ* dynamic response of silt deposits.

Comparison of the Post-cyclic Undrained Shear Strength of Laboratory DSS and In-Situ Tests

Following the stress-controlled cyclic loading phase of DSS tests performed on intact specimens, selected specimens were re-centered and monotonically sheared at rate of 5% per hour under constant-volume conditions to evaluate the post-cyclic undrained shear strength, $s_{u,pcy}$. Figure 12a illustrates examples of post-cyclic normalized shear stress-shear strain responses of selected specimens with various degrees of cyclic shear-induced maximum excess pore pressure ratio and shear strain magnitude. Since the monotonic shear stress-strain response exhibited strain hardening behavior, the post-cyclic undrained shear strength ratio, $s_{u,pcy}/\sigma'_{vc}$, was set equal to the shear strength mobilized at 15% shear strain (Dahl et al. 2014). The variation of $s_{u,pcy}/\sigma'_{vc}$ with $r_{u,max}$ is shown in Fig. 12b. On average, the static s_u/σ'_{vc} of 0.49 degrades to 0.29 for $r_{u,max}$ = 85%.

Vane shear tests were conducted within the silt deposit immediately following the Shallow Blast Program. A water- and drilling mud-filled access casing was installed within borehole V-2 (Figure 1a) to a depth of approximately 9 m to facilitate execution of the VSTs within the raised excess pore pressure field and prior to substantial dissipation. The two successful post-blast VSTs conducted at depths of 9.64 and 10.14 m exhibited $s_{u,VST}$ equal to 39.3 and 37.8 kPa, respectively, associated with $r_{u,max}$ = 31% and residual excess pore pressure ratios of 12.6 to 17.5%. The $s_{u,VST}/\sigma'_{vc}$ in the silt deposit reduced from an average of 0.57 to approximately 0.39. Figure 12b compares variation of $s_{u,pcy}/\sigma'_{vc}$ with $r_{u,max}$ derived from the *in-situ* and laboratory investigation of the overconsolidated, alluvial plastic silt deposit and indicated that the post-blast $s_{u,VST}/\sigma'_{vc}$ follow the general trend determined from the DSS test results. Comparison to the mean $s_{u,pcy}/\sigma'_{vc}$ derived from 18 normally-consolidated, reconstituted soils of different plasticity reported by Ajmera et al. (2019) in Figure 12b indicates that the general rate in the reduction in $s_{u,pcy}/\sigma'_{vc}$ with $r_{u,max}$ is similar, though the magnitude of overconsolidation and natural soil fabric contributes to an increased overall post-cyclic strength.

CONCLUDING REMARKS

Three controlled blasting experiments were conducted at the Port of Portland to evaluate the *in-situ*, nonlinear-inelastic, coupled fluid-mechanical response of an instrumented plastic silt deposit to form the basis for comparison to laboratory test data derived for the same deposit. Ground motions associated with controlled blasting were characterized to understand the influence of different body wave components on the dynamic soil response. The three blast events described herein were used to construct the relationship between shear strain, excess pore pressure, and shear modulus degradation of the deposit. These *in-situ* dynamic responses are compared with those observed in conventional laboratory tests to identify the similarities and differences in their behavior. Based on the results of the controlled blasting field campaign, the following may be concluded for the alluvial, plastic silt deposit:

1. Owing to their high frequency nature, the passage of *P-waves* produced elastic excess pore pressures and did not produce residual excess pore pressure in the silt;
2. Near- and far-field *SV* waves components of the ground motions produced the maximum shear strain in the silt due to their low frequency content, which lies in the range of earthquake ground motions. The maximum particle displacements, shear strains, and corresponding residual excess pore pressures generated in the silt are correlated in time and frequency with the low-frequency SV-*waves*;
3. The *in-situ* test results indicated that the threshold shear strain to enter the nonlinear-elastic constitutive regime, γ_{te}, for the silt deposit ranged from 0.002 to 0.003%;

4. The threshold shear strain to enter the nonlinear-inelastic constitutive regime, γ_{tp}, and generate excess pore pressure ranged from 0.008 to 0.012% for the initial dynamic loading, similar to that observed in the corresponding strain-controlled cyclic DSS tests. The shear modulus reduced to approximately 0.71 to 0.74G_{max} upon the triggering of residual excess pore pressure. Subsequent dynamic loading appeared to double the threshold shear strain to generate excess pore pressure indicating a change in the constitutive soil response following dissipation of blast-induced residual excess pore pressures;
5. The *in-situ* test results predict slightly greater excess pore pressure generation in the plastic silt as compared to the laboratory investigation. This observation may point to the role of pore pressure migration governed by the natural system-response. Cyclic elemental tests conducted in the laboratory were unable to capture the redistribution of excess pore pressures *in-situ*;
6. Drainage and excess pore pressure migration appears to have contributed to a stiffer large-strain response than otherwise expected from laboratory-derived shear modulus reduction curves; and,
7. The trend in post-cyclic undrained shear strength with the maximum excess pore pressure ratio derived from DSS test results confirm the observed post-blast *in-situ* vane shear strength.

The experimental controlled blasting technique described herein produced particle velocity amplitudes that ranged from small to large, and resulted in the intended linear-elastic to nonlinear-inelastic dynamic response. This technique holds the potential to achieve any desired magnitude of seismic loading using appropriate distributions of charge weights and distances. Controlled blasting can demonstrate the fundamental dynamic response of any kind of soil and at any depth *in-situ* and therefore can be leveraged to answer pertinent outstanding questions in the geotechnical earthquake engineering profession.

ACKNOWLEDGMENTS

The authors gratefully acknowledge the sponsorship of this work by Cascadia Lifelines Program (CLiP) and its members, with special thanks to member agency Port of Portland. The research presented within this work was made possible by the vision and leadership of Tom Wharton, P.E. (OR) of the Port of Portland, who encouraged and facilitated this work. The Oregon Department of Transportation provided funding to conduct the vane shear tests, and this support is gratefully acknowledged. The authors were also supported by the National Science Foundation (Grant CMMI 1663654) on similar work during the course of these experiments. Thanks are due to the following Oregon State University professional faculty, staff, and students who engaged in discussions and/or assisted with various portions of, or related to, the overall project: T. Matthew Evans, Anne Trehu, James Batti, Aleyna Donaldson, Erick Moreno-Rangel, and Ali Dadashi. The authors thank Kenneth H. Stokoe II, Brady R. Cox, Farnyuh Menq, and Benchen Zhang for fruitful discussions.

DECLARATIONS OF INTEREST

Declarations of interest: None.

REFERENCES

Adamidis, O., and Madabhushi, S.P.G. 2018. Experimental investigation of drainage during earthquake-induced liquefaction. Geotechnique, 68(8): 655–665.

Ajmera, B., Brandon, T., and Tiwari, B. 2019. Characterization of the Reduction in Undrained Shear Strength in Fine-Grained Soils due to Cyclic Loading. J. Geotech. Geoenviron. Eng., 145(5), 04019017.

ASTM D7400-19. 2019. Standard Test Methods for Downhole Seismic Testing, ASTM International, West Conshohocken, PA.

Beyzaei, C. Z., Bray, J. D., Cubrinovski, M., Bastin, S., Stringer, M., Jacka, M., and Wentz, R.

2019. Characterization of silty soil thin layering and groundwater conditions for liquefaction assessment. Canadian Geotechnical Journal, 57(2): 263-276.

Beyzaei, C. Z., Bray, J. D., Cubrinovski, M., Riemer, M., and Stringer, M. 2018. Laboratory-based characterization of shallow silty soils in southwest Christchurch. Soil Dynamics and Earthquake Engineering, 110: 93-109.

Blair, D. 2010. Seismic radiation from an explosive column. Geophysics, 75(1): E55-E65.

Blair, D. 2015. The free surface influence on blast vibration. International Journal of Rock Mechanics and Mining Sciences, 77: 182-191.

Boulanger, R.W., and Idriss, I. M. 2007. Evaluation of cyclic softening in silts and clays. J. Geotech. Geoenviron. Eng., 133(6): 641– 652

Boulanger, R.W., Meyers, M. W., Mejia, L. H., and Idriss, I. M. 1998. Behavior of a fine-grained soil during the Loma Prieta earthquake. Canadian Geotechnical Journal, 35(1): 146-158.

Bray, J.D. and Sancio, R.B. 2006. Assessment of the Liquefaction Susceptibility of Fine-Grained Soils, J. Geotech. Geoenv. Engrg., 132(9):1165-1177.

Cappa, R., Brandenberg, S.J., and Lemnitzer, A. 2017. Strains and pore pressures generated during cyclic loading of embankments on organic soil. J. Geotech. Geoenviron. Eng., 143 (9): 04017069.

Chandrupatla, T. R., Belegundu, A. D., Ramesh, T., and Ray, C. 2002. Introduction to finite elements in engineering (Vol. 10). Upper Saddle River, NJ: Prentice Hall.

Chang, W. J., Rathje, E. M., Stokoe, K. H., II, and Hazirbaba, K. 2007. In Situ Pore Pressure Generation Behavior of Liquefiable Sand. J. Geotech. Geoenviron. Eng., 133: 921–931.

Charlie, W. A., Bretz, T.E., Schure, L.A., and Doehring, D.O. 2013. Blast-Induced Pore Pressure and Liquefaction of Saturated Sand. J. Geotech. Geoenviron. Eng., 139(8):1308-1319.

Charlie, W.A., Jacobs, P.J., and Doehring, D.O. 1992. Blast induced liquefaction of an alluvial sand deposit. Geotechnical Testing Journal, 15(1): 14–23.

Cox, B.R., Stokoe, K., and Rathje, E. 2009. An in -situ test method for evaluating the coupled pore pressure generation and nonlinear shear modulus behavior of liquefiable soils. Geotechnical Testing Journal, 32(1): 11-21.

Cox, B.R. 2006. Development of a direct test method for dynamically assessing the liquefaction resistance of soils in situ. PhD Thesis, University of Texas at Austin, 498 pp.

Cubrinovski, M., Rhodes, A., Ntritsos, N., Van Ballegooy, S. 2019. System response of liquefiable deposits. Soil Dynamics and Earthquake Engineering, 124: 212-229.

Dahl, K. R., Boulanger, R. W., DeJong, J. T., and Driller, M. W. 2010. Effects of sample disturbance and consolidation procedures on cyclic strengths of intermediate soils. in 5th Int. Conf. Recent Adv. Geotech. Earthq. Engrg. and Soil Dyn. and Symposium in Honor of Professor I. M. Idriss, San Diego, CA, May, Paper No OSP1, 1-20, 2010.

Dahl, K.R., DeJong, J.T., Boulanger, R.W., Pyke, R. and Wahl, D., 2014. Characterization of an alluvial silt and clay deposit for monotonic, cyclic, and post-cyclic behavior. Canadian Geotechnical Journal, 51(4): 432-440.

Darendeli, M. B., 2001. Development of a new family of normalized modulus reduction and material damping curves. PhD dissertation, Univ. of Texas at Austin, Austin, Texas.

DeJong, J. T., C. P. Krage, B. A. Albin, and D. J. DeGroot. 2018. A work based framework for sample quality evaluation of low plasticity soils. J. Geotech. Geoenviron. Eng., 144 (10): 04018074

Dobry, R., and Abdoun, T. 2015. Cyclic shear strain needed for liquefaction triggering and assessment of overburden pressure factor k σ. J. Geotech. Geoenviron. Eng., 141(11): 04015047.

Donaldson, A.M. 2019. Characterization of the Small-Strain Stiffness of Soils at an In Situ Liquefaction Test Site. MS Thesis, Oregon State University, 287 pp.

Dowding, C. H., and Duplaine, H. 2004. State of the art in blast densification or explosive compaction. ASEP-GI 2004, 2.

Dyvik, R., Berre, T., Lacasse, S., and Raadim, B. 1987. Comparison of truly undrained and constant volume direct simple shear tests. Geotechnique, 37(1): 3-10.

Fragaszy Richard, J., and Voss, M.E. 1986. Undrained Compression Behavior of Sand. Journal of Geotechnical Engineering, 112(3): 334-347.

Gao, Q., Lu, W., Yang, Z., Yan, P., and Chen, M. 2019. Analysis of evolution of seismic components induced by a vertical blasthole. Rock Mechanics and Rock Engineering, 52(6): 1959-1977.

Gianella, T., and Stuedlein, A.W. 2017. Performance of Driven Displacement Pile–Improved Ground in Controlled Blasting Field Tests. J. Geotech. Geoenviron. Eng., 143(9): 04017047.

Gohl, W. B., Howie, J. A., and Rea, C. E. 2001. Use of controlled detonation of explosives for liquefaction testing. Proc., 4th Int. Conf. on Recent Advances in Geotechnical Earthquake Engineering and Soil Dynamics, Univ. of Missouri-Rolla, Rolla, MO.

Hashash, Y., Phillips, C., and Groholski, D.R. (2010). Recent advances in non-linear site response analysis. Proc., 5th Int. Conf. on Recent Advances in Geotechnical Earthquake Engineering and Soil Dynamics, Univ. of Missouri-Rolla, Rolla, MO.

Heelan, P.A. 1953. Radiation from a cylindrical source of finite length. Geophysics, 18(3): 685.

Hryciw, R. D. 1986. A Study of the Physical and Chemical Aspects of Blast Densification of Sand, PhD Thesis, Northwestern University, Evanston, IL, 229 pp.

Hsu, C.C. and Vucetic, M. 2006. Threshold shear strain for cyclic pore-water pressure in cohesive soils. J. Geotech. Geoenviron. Eng., 132(10):1325-1335.

Ichii, K., & Mikami, T. 2018. Cyclic threshold shear strain in pore water pressure generation in clay in situ samples. Soils and foundations, 58(3): 756-765.

Ishihara, K. 1967. Propagation of compressional waves in a saturated soil. *In* Proc. Int. Symp.

Wave Progapation and Dynamic Properties of Earth Materials, pp. 195-206.

Jana, A., and Stuedlein, A.W. 2021. Dynamic *In-Situ* Response of a Deep, Medium Dense Sand Deposit Deposit. J. Geotech. Geoenviron. Eng., *In Press.*

Jana, A., and Stuedlein, A.W. 2020. Monotonic, Cyclic and Post-Cyclic Response of an Alluvial Plastic Silt Deposit. J. Geotech. Geoenviron. Eng., 147(12), 04020174.

Jana, A., Donaldson, A. M., Stuedlein, A. W., and Evans, T. M. 2021. "Deep, *In-Situ* Nonlinear Dynamic Testing of Soil with Controlled Blasting: Instrumentation, Calibration, and Example Application to a Plastic Silt Deposit, Geotechnical Testing Journal, 44(5), GTJ20190426.

Kramer, S. L., Sideras, S. S., and Greenfield, M. W. 2016. The timing of liquefaction and its utility in liquefaction hazard evaluation. Soil Dynamics and Earthquake Engineering, 91: 133-146.

Kurtulus, A., and Stokoe, K. H. (2008). In situ measurement of nonlinear shear modulus of silty soil. J. Geotech. Geoenviron. Eng., 134(10): 1531-1540.

Lunne, T., Berre, T., Andersen, K. H., Strandvik, S., and Sjursen, M. 2006. Effects of sample disturbance and consolidation procedures on measured shear strength of soft marine Norwegian clays. Canadian Geotechnical Journal, 43(7): 726-750.

Markham, C.S., Bray, J.D., Macedo, J., and Luque, R. (2016). Evaluating nonlinear effective stress site response analyses using records from the Canterbury earthquake sequence. Soil Dynamics and Earthquake Engineering, 82, 84-98.

Mayne, P.W. 2007. Cone penetration testing: A synthesis of highway practice. NCHRP Report, No. 368. Transportation Research Board, Washington, D.C

Mortezaie, A. and Vucetic, M., 2016. Threshold shear strains for cyclic degradation and cyclic pore water pressure generation in two clays. J. Geotech. Geoenviron. Eng., 142(5): 04016007.

Narin Van Court, W. A., and Mitchell, J. K. 1994. Soil improvement by blasting. Journal of Explosives Eng. 12 (3): 34-41.

Ni, M., Abdoun, T., Dobry, R., Zehtab, K., Marr, A., and El-Sekelly, W. 2020. Pore Pressure and K σ Evaluation at High Overburden Pressure under Field Drainage Conditions. I: Centrifuge Experiments. J. Geotech. Geoenviron. Eng., 146(9): 04020088.

Roberts, J.N., Stokoe, K.H., II, Hwang, S., Cox, B.R., Wang, Y., Menq, F.M., and van Ballegooy, S. 2016, Field measurements of the variability in shear strain and pore pressure generation in Christchurch soils, *In* Proc., 5th Int. Conf. on Geotechnical and Geophysical Site Characterisation, ICS (5).

Robertson, P. 2009. Interpretation of cone penetration tests – a unified approach. Canadian Geotechnical Journal, 46(11): 1337–1355.

Sanchez-Salinero, I., Roesset, J. M., and Stokoe, K.H. 1986. Analytical studies of body wave propagation and attenuation. Technical Report GR86-15, University of Texas, Austin.

Sanin, M.V., and Wijewickreme, D. 2006. Cyclic shear response of channel-fill Fraser River Delta silt. Soil Dynamics and Earthquake Engineering, 26: 854– 869.

Seed, H.B. 1979. Soil Liquefaction and Cyclic Mobility Evaluation for Level Ground during Earthquakes, J. Geotech. Engrg. Div, 105 (2): 201-255.

Soysa, A., and Wijewickreme, D. 2019. Repeated cyclic shear loading response of reconstituted Fraser River silt. *In* Proceedings of the 7th International Conference on Earthquake Geotechnical Engineering, Rome, Italy.

Soysa, A.N. 2015. Monotonic and cyclic shear loading response of natural silts. PhD diss., University of British Columbia.

Stockwell, R. G., Mansinha, L., and Lowe, R. P. 1996. Localization of the complex spectrum: the S transform. IEEE Trans. Sig. Proc. 44 (4): 998–1001.

Stokoe, K. H., Roberts, J. N., Hwang, S., Cox, B. R., Menq, F. Y., and Van Ballegooy, S. 2014. Effectiveness of inhibiting liquefaction triggering by shallow ground improvement methods: Initial field shaking trials with T-Rex at one site in Christchurch, New Zealand. *In* Soil liquefaction during recent large-scale earthquakes, 193.

Tabata, K., and Vucetic, M. 2010. Threshold shear strain for cyclic degradation of three clays. *In* Proc. 5th Int. Conf. on Recent Advances in Geotechnical Earthquake Engineering and Soil Dynamics, Missouri Univ. of Science and Technology, Rolla, MO

Van Ballegooy, S., Roberts, J. N., Stokoe, K. H., Cox, B. R., Wentz, F. J., and Hwang, S. 2015. Large-scale testing of shallow ground improvements using controlled staged-loading with T-Rex. *In* Proceedings of the Sixth International Conference on Earthquake Geotechnical Engineering.

Vardanega, P. J., and Bolton, M. D. 2011. Practical methods to estimate the non-linear shear stiffness of clays and silts. Proc., 5th Int. Conf. on the Deformation Characteristics of Geo-materials, IOS Press, Amsterdam, Netherlands, 372–379.

Vardanega, P. J., and Bolton, M. D. 2013. Stiffness of clays and silts: Normalizing shear modulus and shear strain. J. Geotech. Geoenviron. Eng., 139(9): 1575-1589.

Vucetic, M., and Dobry, R. 1991. Effect of soil plasticity on cyclic response. J. Geotech. Engrg., 117(1): 89–107.

Vucetic, M., and Tabata, K. 2003. Influence of soil type on the effect of strain rate on small-strain cyclic shear modulus. Soils Found., 43(5): 161–173.

Wijewickreme, D., A. Soysa, and P. Verma. 2019. Response of Natural Fine-Grained Soils for Seismic Design Practice: A Collection of Research Findings from British Columbia, Canada. Soil Dynamics and Earthquake Engineering, 124: 280-296.

Table 1 Charge weight, depths, and schedule of detonation comprising the three blast programs (refer to Figs. 1a and 3).

Test Blast Program (TBP)				Deep Blast Program (DBP)				Shallow Blast Program (SBP)			
Detonation sequence and charge location	Time (s)	Depth (m)	Charge weight (gm)	Detonation sequence and charge location	Time (s)	Depth (m)	Charge weight (gm)	Detonation sequence and charge location	Time (s)	Depth (m)	Charge weight (gm)
1: CX	0	6.6	227	1: C1	0	23.14	90	1: C6	0	8.21	90
2: CX	1	8.2	454	2: C10	1	13.69	90	2: C15	1	7.29	90
3: CX	2	10.2	907	3: C1	2	25.27	90	3: C6	2	9.73	90
4: CX	3	12.6	1,814	4: C10	3	23.44	90	4: C15	3	9.73	90
5: CX	4	18.2	454	5: C1	4	26.84	150	5: C6	4	11.97	150
6: CX	5	20.2	907	6: C10	5	26.56	150	6: C15	5	11.59	150
7: CX	6	22.6	1,814	7: C2	6	22.79	228	7: C7	6	7.56	228
8: CX	7	25.7	3,628	8: C9	7	22.64	228	8: C14	7	7.56	228
				9: C2	8	24.70	456	9: C7	8	9.28	456
				10: C9	9	24.22	456	10: C14	9	9.89	456
				11: C2	10	26.59	912	11: C7	10	11.29	912
				12: C9	11	26.59	912	12: C14	11	11.77	912
				13: C3	12	19.91	1824	13: C8	12	5.82	1824
				14: C8	13	19.91	1824	14: C13	13	6.20	1824
				15: C3	14	22.66	1824	15: C8	14	8.65	912
				16: C8	15	22.96	1824	16: C13	15	9.16	912
				17: C3	16	25.87	3648	17: C8	16	11.29	912
				18: C8	17	25.87	3648	18: C13	17	11.39	912
				19: C4	18	19.10	3648	19: C9	18	4.10	456
				20: C7	19	19.10	3648	20: C12	19	4.10	456
				21: C4	20	22.39	2721	21: C9	20	7.76	456
				22: C7	21	22.70	2721	22: C12	21	7.76	456
				23: C4	22	26.04	2721	23: C9	22	11.52	228
				24: C7	23	25.74	2721	24: C12	23	11.88	228
				25: C5	24	23.39	1361	25: C10	24	6.66	150
				26: C6	25	21.25	1361	26: C11	25	6.66	150
				27: C5	26	24.15	1361	27: C10	26	9.40	150
				28: C6	27	24.00	1361	28: C11	27	9.40	150
				29: C5	28	26.53	912	29: C10	28	11.54	150
				30: C6	29	26.53	912	30: C11	29	11.95	150

Table 2. Threshold shear strain to trigger excess pore pressure observed in the blast programs.

	Test Blast		Shallow Silt Blast	
Element	Threshold shear strain to trigger excess pore pressure, γ_{tp} (%)	Residual excess pore pressure ratio, $r_{u,r}$ (%)	Threshold shear strain to trigger excess pore pressure, γ_{tp} (%)	Residual excess pore pressure ratio, $r_{u,r}$ (%)
1	0.012	0.35	0.021	0.24
2	0.008	0.73	0.015	0.84
3	0.016	0.10	0.029	0.37
4	0.011	0.10	0.028	0.37

Table 3 Downhole small-strain shear wave velocity of the Silt Array prior to the Test and Shallow Blast Programs .

TGP Pair	Borehole	Range in depth (m)	Average V_s prior to TBP (m/s)	Average V_s prior to SBP (m/s)
S3 and S4	B-6	9.0 to 10.2	125	151
S4 and S5	B-6	10.2 to 11.5	126	137
S3 and S5	B-6	9.0 to 11.5	126	139
S6 and S7	B-4	9.0 to 10.2	119	124
S7 and S8	B-4	10.2 to 11.4	154	137
S6 and S8	B-4	9.0 to 11.2	136	131

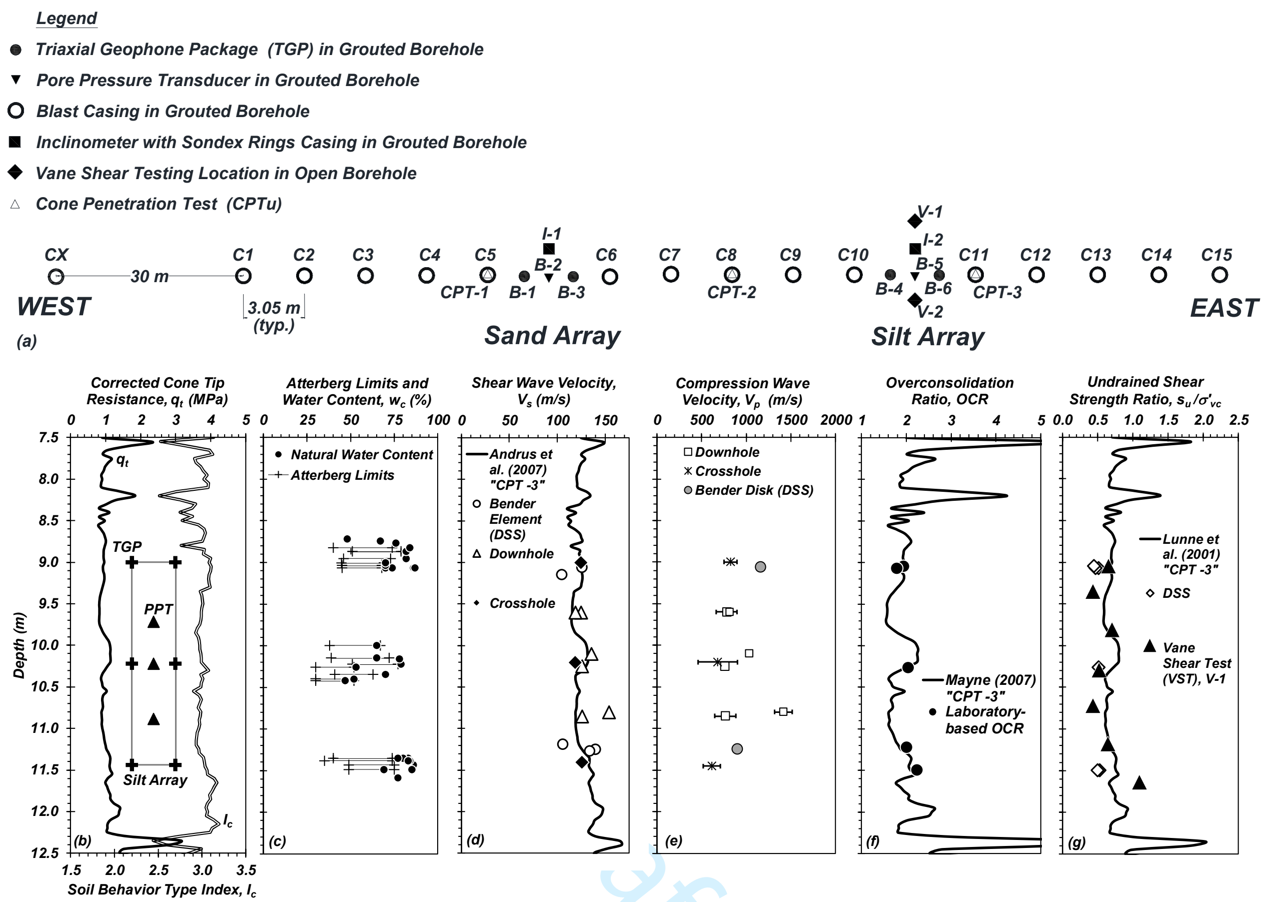

Figure 1. Test site and subsurface conditions: (a) site and exploration plan indicating blast casings and instruments comprising the Sand and Silt Arrays, (b) cone tip resistance and soil behavior type index (CPT-3), (c) natural water content and Atterberg limits, (d) comparison of *in-situ* shear wave and (e) compression wave velocity measurements with those corresponding to intact DSS test specimens, (f) overconsolidation ratio and (g) undrained shear strength ratio and their correlations to the CPT (site-specific $N_k = 10$; Lunne et al. 2001; modified from Jana et al. 2021 with permission © ASTM International).

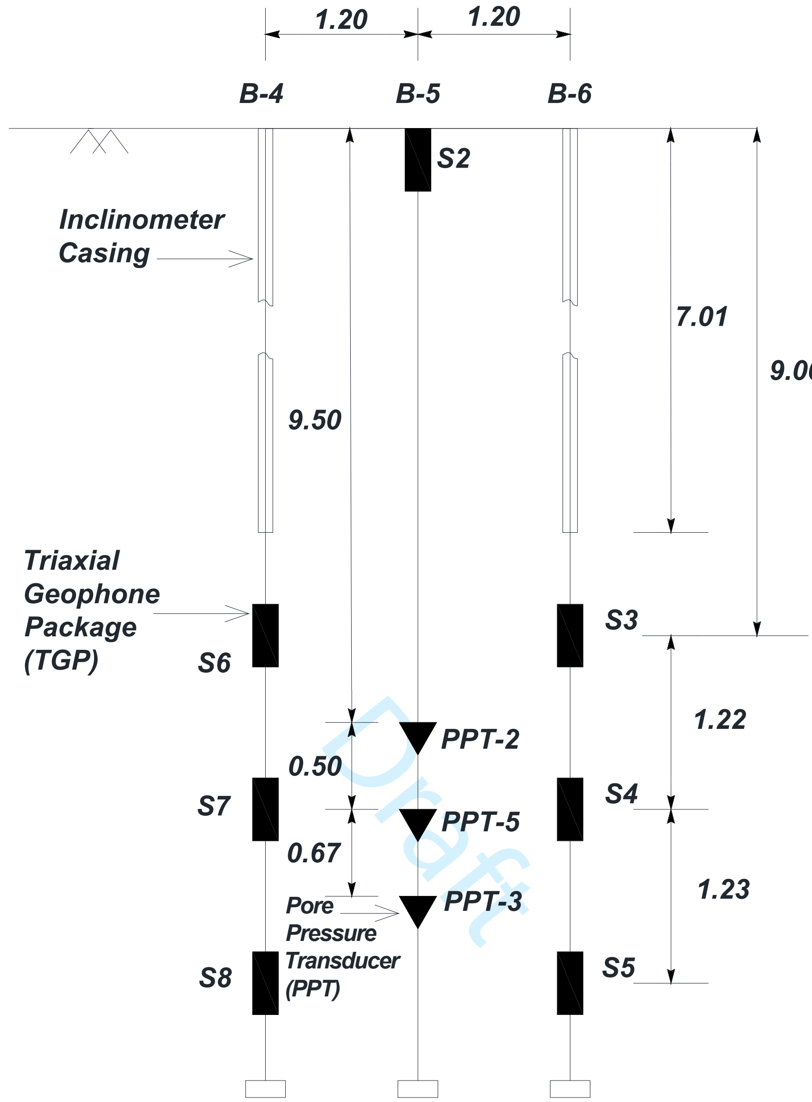

Figure 2. Elevation view of the Silt array comprising various instruments, including triaxial geophone packages (TGP), pore pressure transducers (PPT), and inclinometer casing. Inclinometer casing with sondex rings, I-2, not shown here for clarity (all units in m; modified from Jana et al. 2021 with permission © ASTM International).

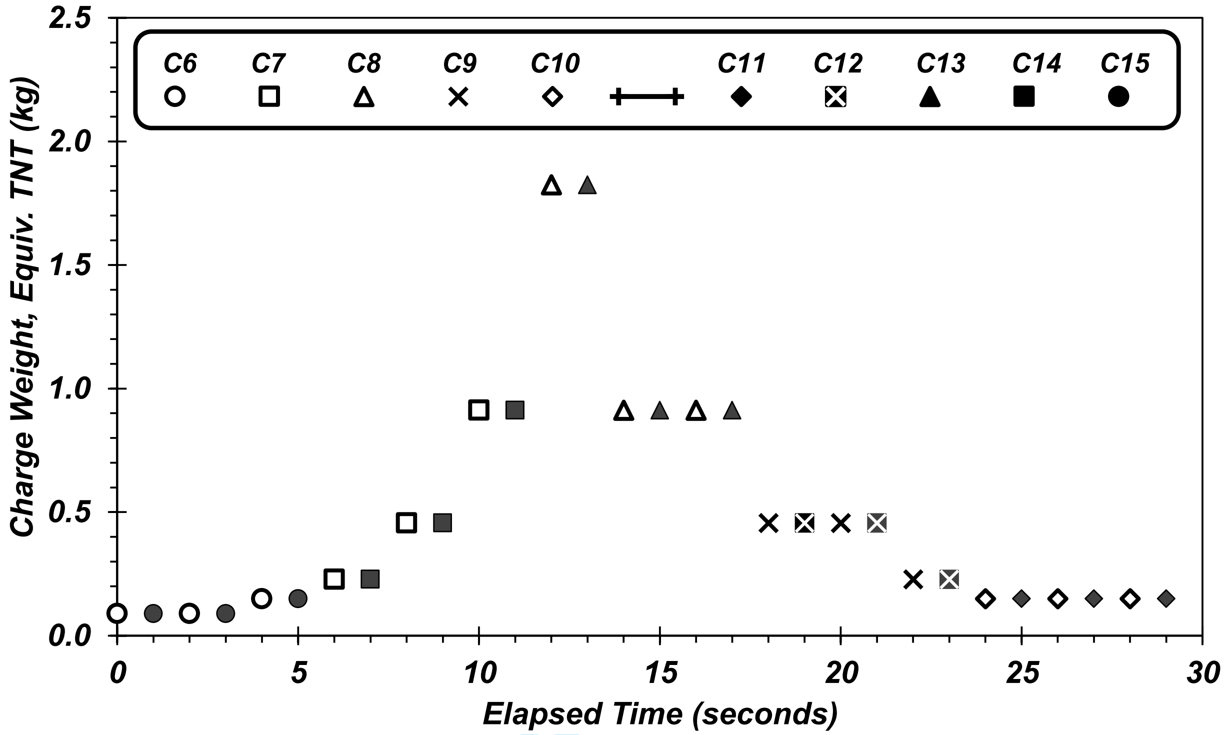

Figure 3. Charge weight detonation time history conducted during the Shallow Blast program (SBP) indicating their distribution within blast casings C6 through C15 (compare to Fig. 1a and Table 1).

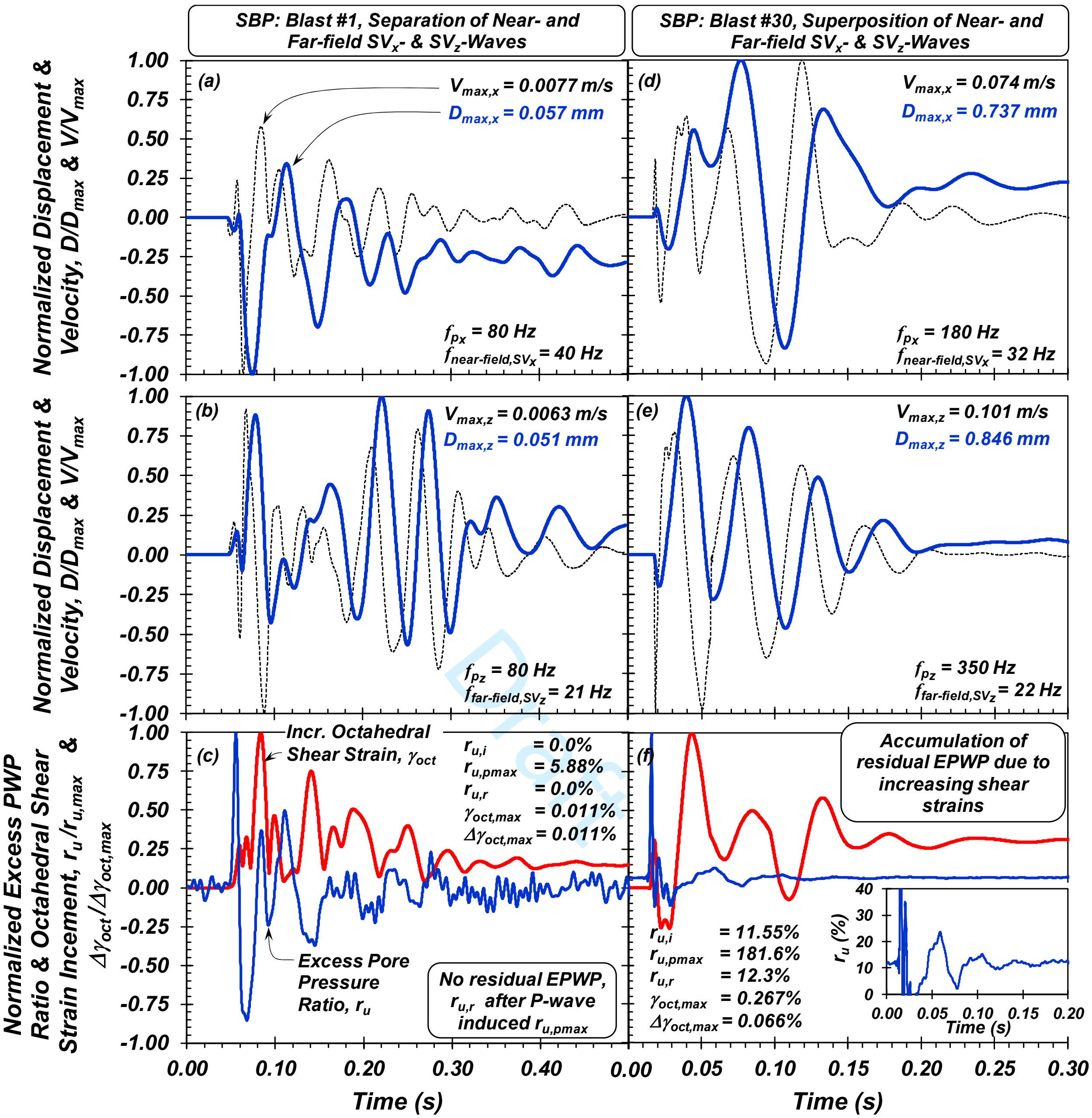

Figure 4. Normalized velocity and displacement in the (a) horizontal and (b) vertical direction for a 90 gram charge detonated at a distance 16.5 m from TGP S3, and (c) corresponding normalized octahedral shear strain increment and excess pore pressure ratio in Element 1, (d) normalized velocity and displacement in the (d) horizontal and (e) vertical direction for a 150 gram charge detonated at a distance 3.5 m from TGP S3, and (f) corresponding normalized octahedral shear strain increment and excess pore pressure ratio in Element 1.

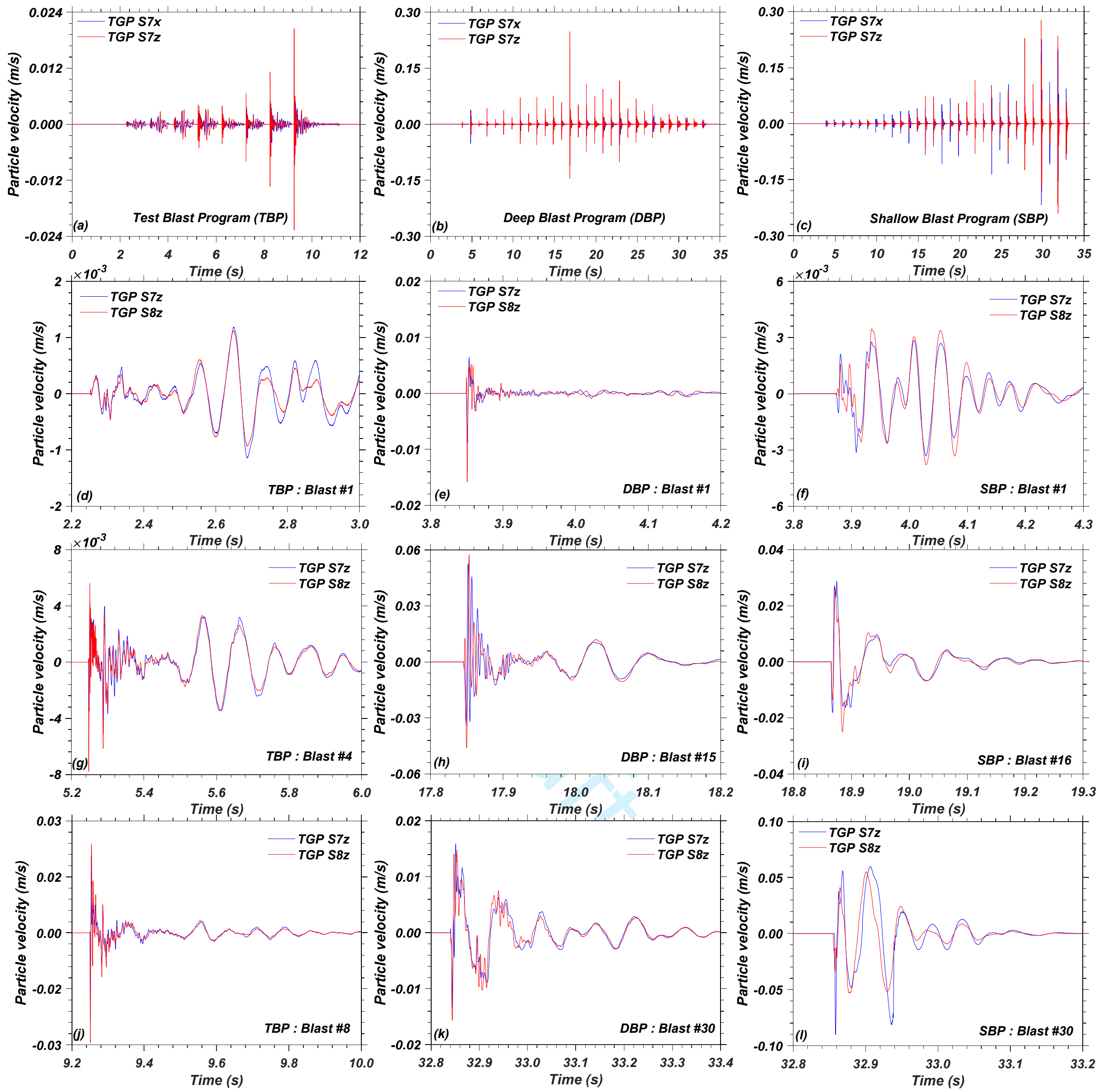

Figure 5. Examples of particle velocity time histories recorded in TGP 7 during the: (a) Test Blast Program (TBP), (b) Deep Blast Program (DBP), and (c) Shallow Blast Program (SBP); and comparison of the body wave amplitudes and phases of two vertically-separated geophones located within the same borehole: (d) TBP Blast #1, (e) DBP Blast #1, (f) SBP Blast #1, (g) TBP Blast #4, (h) DBP Blast #15, (i) SBP Blast #16, (j) TBP Blast #8, (k) DBP Blast #30, and (l) SBP Blast #30.

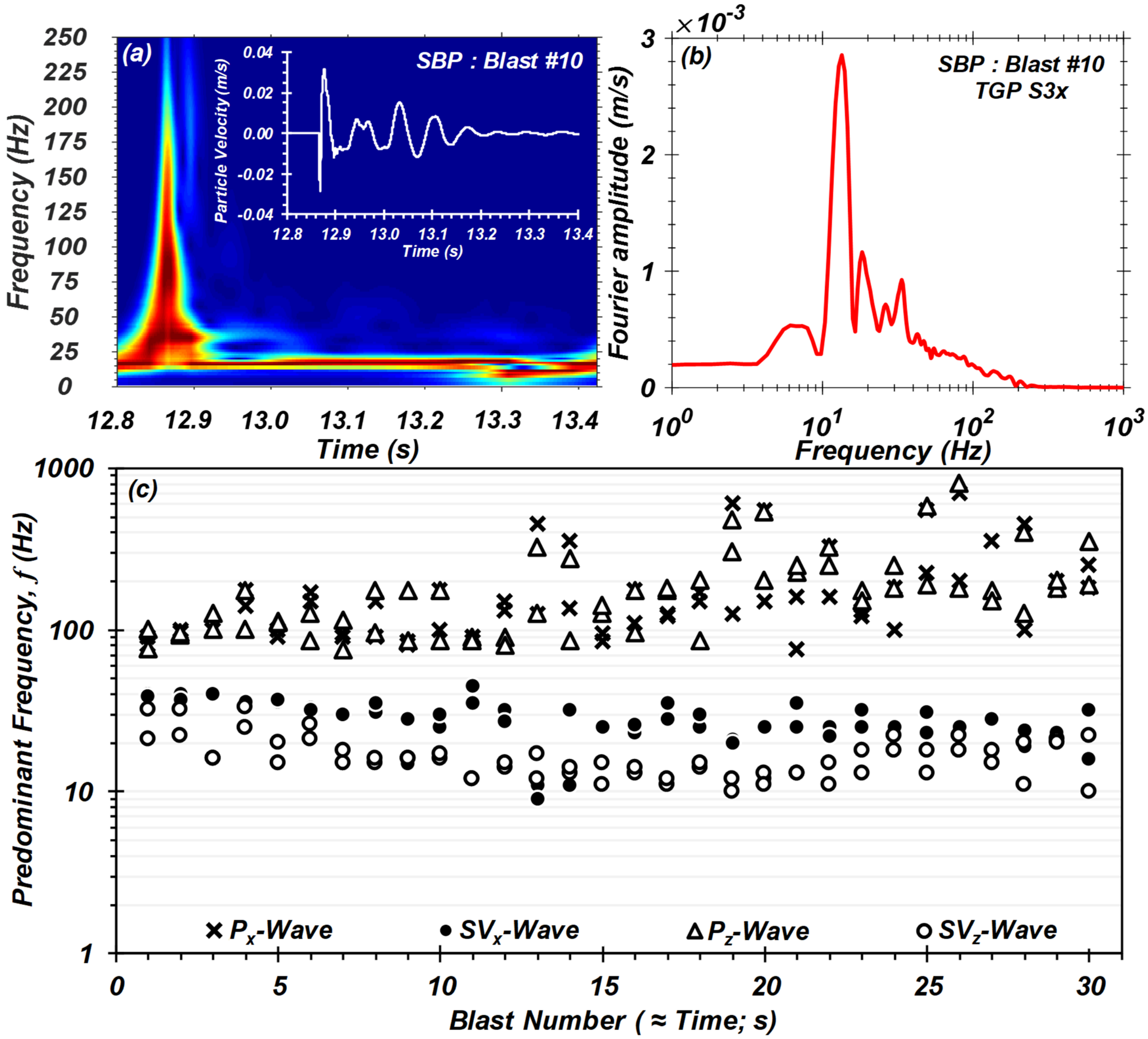

Figure 6. Frequency content of blast-induced ground motions: (a) normalized Stockwell spectrogram showing variation of frequency content of the body wave components over time, (b) Fourier amplitude spectrum of particle velocity for TGP S3x during SBP Blast #10, and (c) variation of predominant frequency of *P-wave*, *SV_x-wave* (near-field) and *SV_z-wave* (far-field) during the Shallow Blast Program from two representative TGPs.

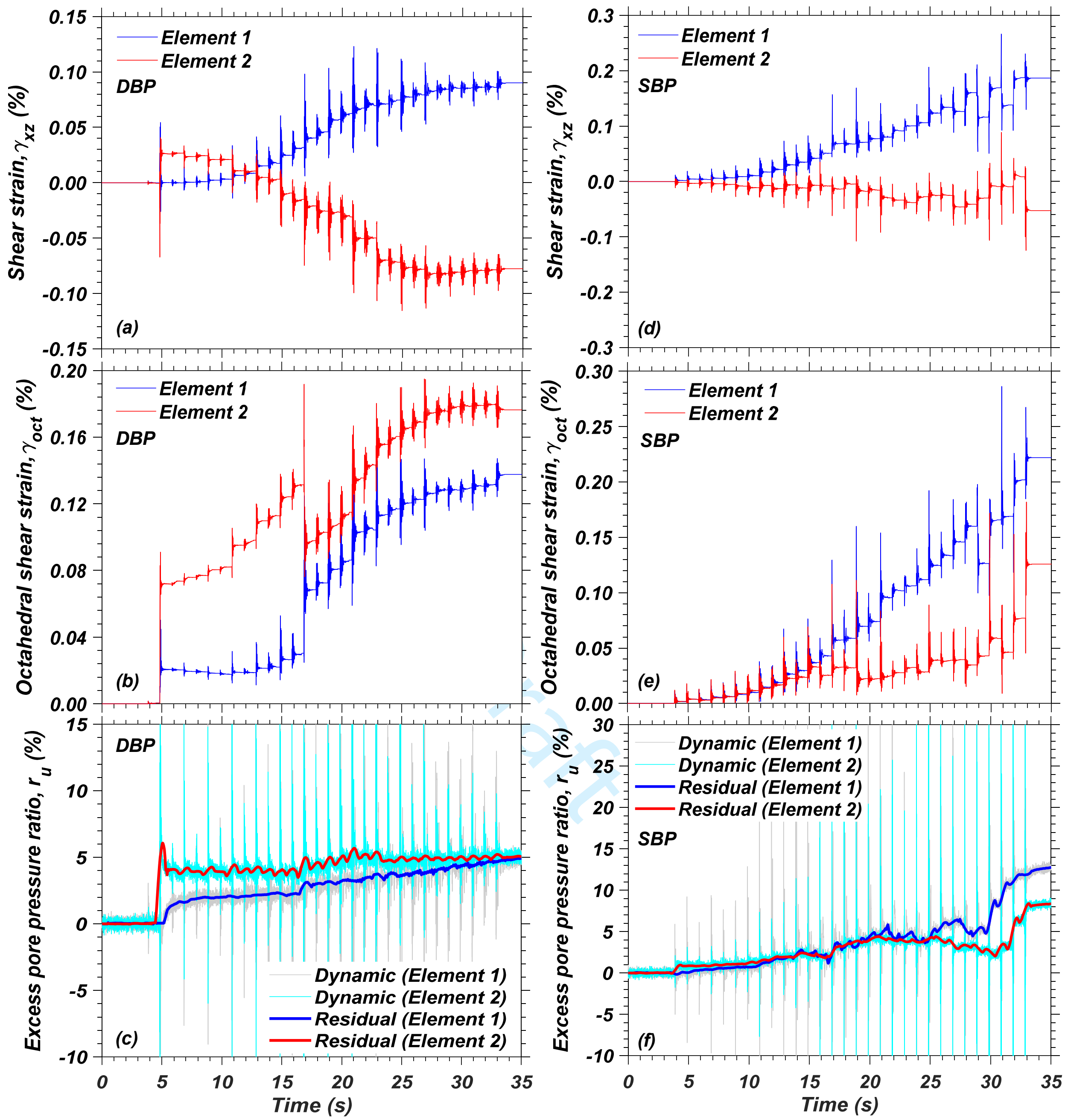

Figure 7. Dynamic response of the Silt Array including the variation of the: (a) Cauchy shear strain, γ_{xz}, (b) octahedral shear strain, γ_{oct}, and (c) excess pore pressure ratio, r_u, time histories for the Deep Blast Program, and the: (d) γ_{xz}, (e) γ_{oct}, and (f) r_u time histories for Shallow Blast Program.

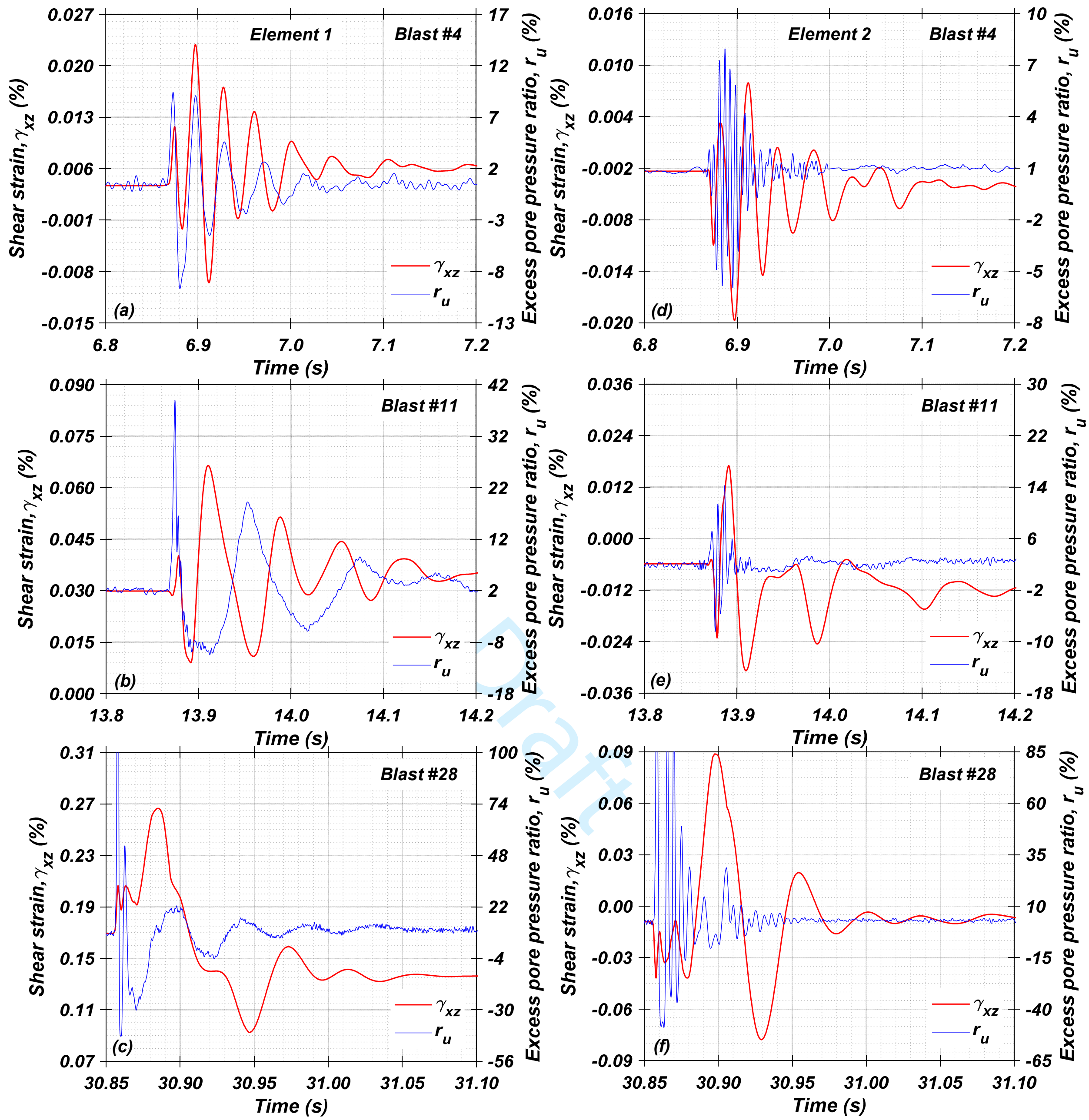

Figure 8. Example of Cauchy shear strain, γ_{xz} and corresponding excess pore pressure ratio, r_u, time histories observed in the Silt Array at Elements 1 and 2 for the various charge detonations during the Shallow Blast Program: (a) – (c) Element 1 (PPT-2), (d) – (e) Element 2 (PPT-3).

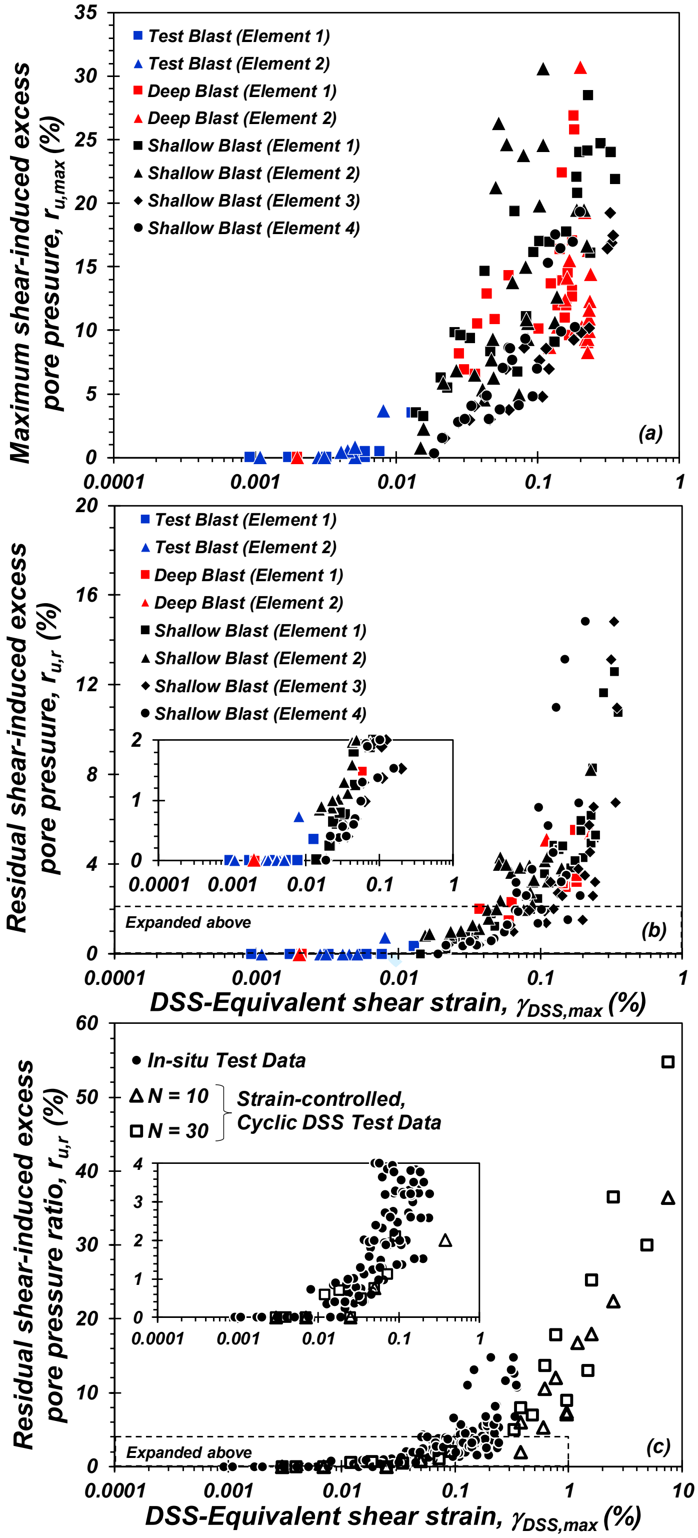

Figure 9. Variation of excess pore pressure, r_u, and maximum DSS-equivalent shear strain, $\gamma_{DSS,max}$, deduced for the Silt Array during the Test (TBP), Deep (DBP), and Shallow Blast Programs (SBP): (a) maximum shear-induced excess pore pressure ratio, $r_{u,max}$, and (b) residual shear-induced excess pore pressure ratio, $r_{u,r}$, with $\gamma_{DSS,max}$, and (c) comparison of $r_{u,r}$ from *in-situ* tests and intact DSS test specimens.

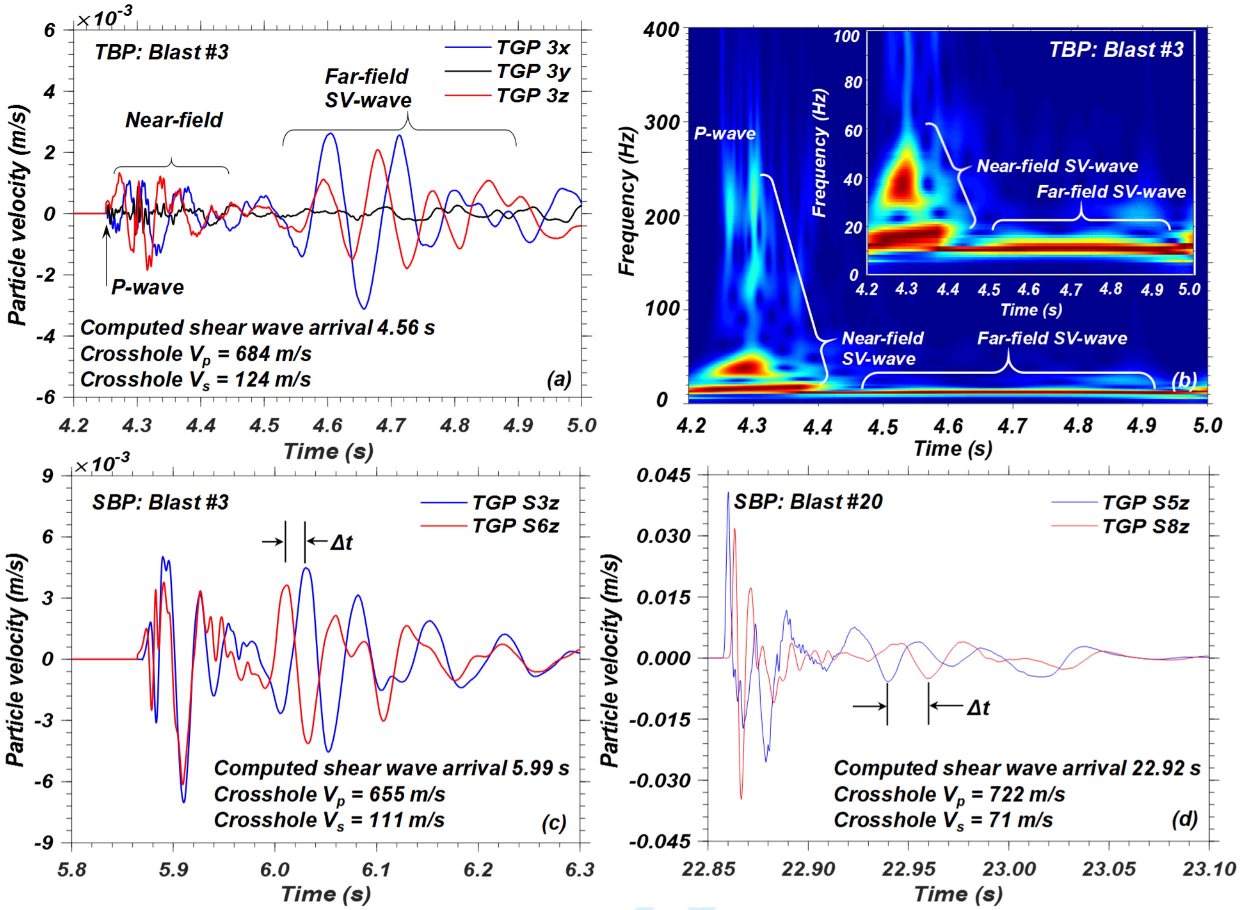

Figure 10. Body wave component identification and velocities: (a) example of an orthogonal, three-component velocity time history (TGP S3, #3) and (b) corresponding normalized Stockwell spectrogram (TGP S3x); and comparison of the vertical body wave amplitudes and phases of two horizontally-separated geophones: (c) SBP Blast #3 observed in TGPs 3 and 6, and (d) SBP Blast #20 observed in TGPs 5 and 8.

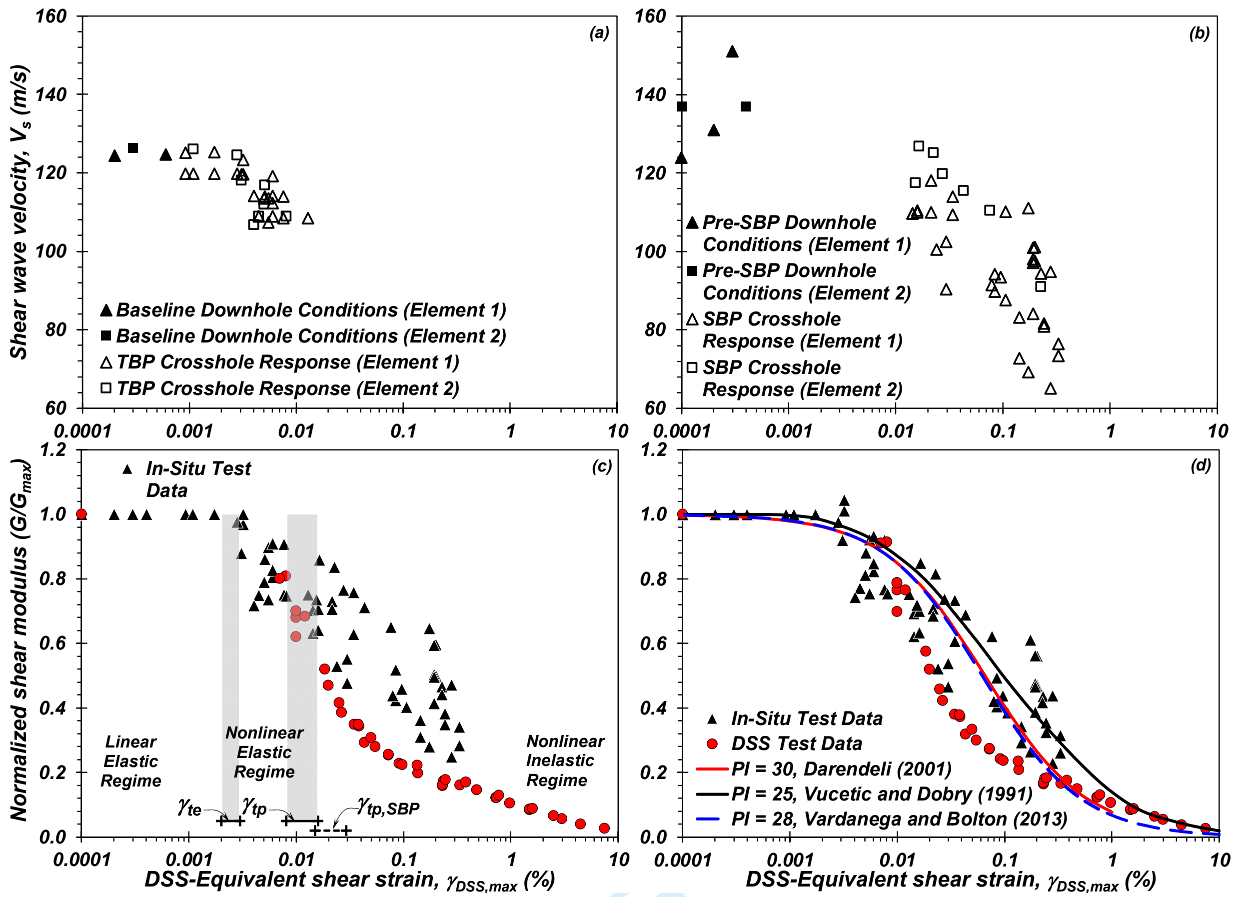

Figure 11. Variation of shear wave velocity, V_s, with $\gamma_{DSS,max}$ in the Silt Array for the: (a) Test Blast Program (TBP), and (b) Shallow Blast Program (SBP); and, comparison of the: (c) measured *in-situ* shear modulus degradation and strain-controlled DSS test data for intact specimens (N = 1) with $\gamma_{DSS,max}$ and threshold shear strains identified, and (d) strain rate-corrected G/G_{max} with $\gamma_{DSS,max}$ (f = 1 Hz).

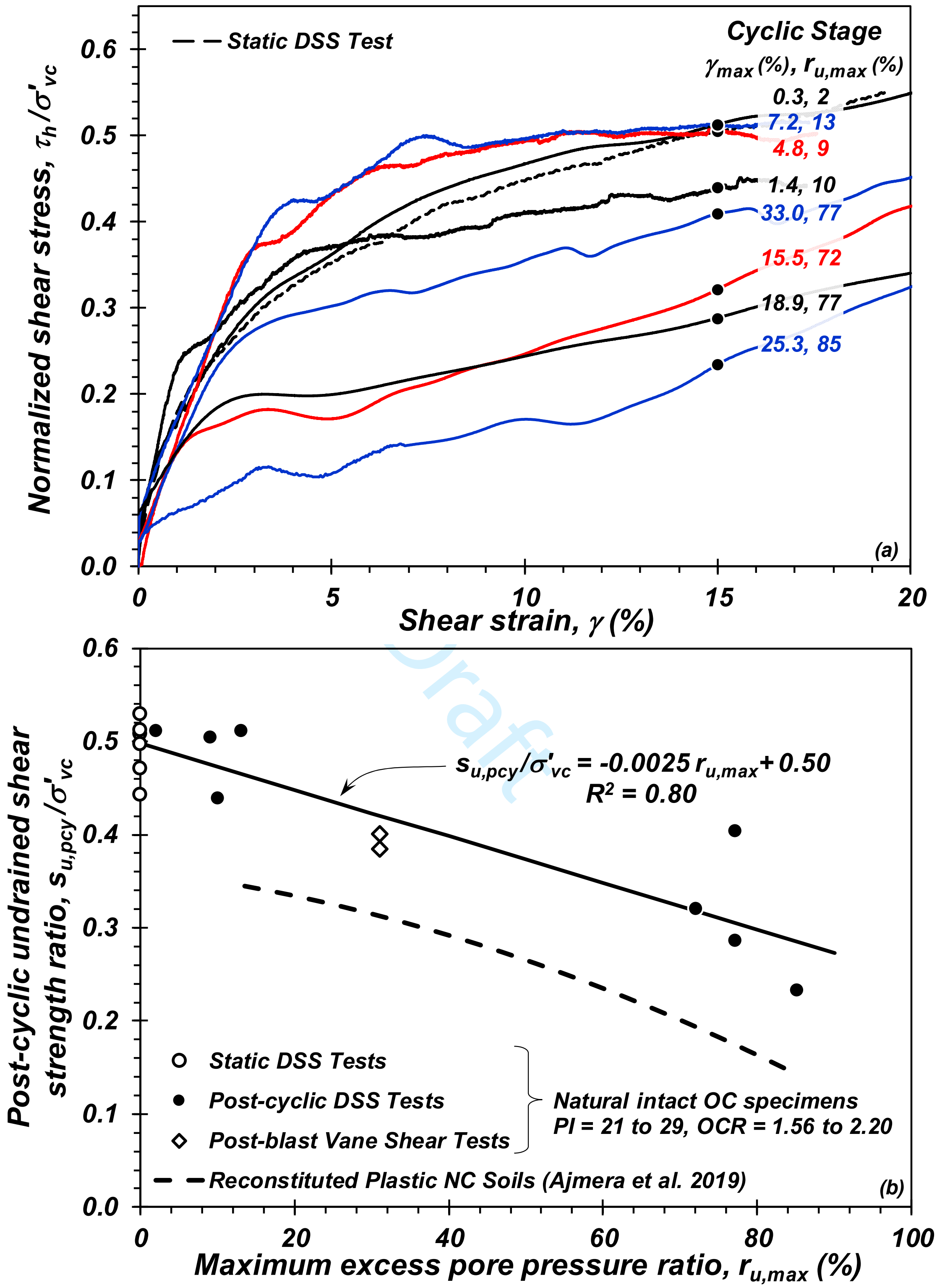

Figure 12. Effect of excess pore pressures on undrained shear strength: (a) normalized, post-cyclic, constant-volume, monotonic shear stress-shear strain response from DSS tests on natural, intact specimens, and (b) variation of post-cyclic DSS and post-blast vane shear test normalized undrained shear strength ratio with cyclic and blast-induced, *in-shear* maximum excess pore pressure ratio.

Figure 1. Test site and subsurface conditions: (a) site and exploration plan indicating blast casings and instruments comprising the Sand and Silt Arrays, (b) cone tip resistance and soil behavior type index (CPT-3), (c) natural water content and Atterberg limits, (d) comparison of *in-situ* shear wave and (e) compression wave velocity measurements with those corresponding to intact DSS test specimens, (f) overconsolidation ratio and (g) undrained shear strength ratio and their correlations to the CPT (site-specific $N_k = 10$; Lunne et al. 2001; modified from Jana et al. 2021 with permission © ASTM International).

Figure 2. Elevation view of the Silt array comprising various instruments, including triaxial geophone packages (TGP), pore pressure transducers (PPT), and inclinometer casing. Inclinometer casing with sondex rings, I-2, not shown here for clarity (all units in m; modified from Jana et al. 2021 with permission © ASTM International).

Figure 3. Charge weight detonation time history conducted during the Shallow Blast program (SBP) indicating their distribution within blast casings C6 through C15 (compare to Fig. 1a and Table 1).

Figure 4. Normalized velocity and displacement in the (a) horizontal and (b) vertical direction for a 90 gram charge detonated at a distance 16.5 m from TGP S3, and (c) corresponding normalized octahedral shear strain increment and excess pore pressure ratio in Element 1, (d) normalized velocity and displacement in the (d) horizontal and (e) vertical direction for a 150 gram charge detonated at a distance 3.5 m from TGP S3, and (f) corresponding normalized octahedral shear strain increment and excess pore pressure ratio in Element 1.

Figure 5. Examples of particle velocity time histories recorded in TGP 7 during the: (a) Test Blast Program (TBP), (b) Deep Blast Program (DBP), and (c) Shallow Blast Program (SBP); and comparison of the body wave amplitudes and phases of two vertically-separated geophones

located within the same borehole: (d) TBP Blast #1, (e) DBP Blast #1, (f) SBP Blast #1, (g) TBP Blast #4, (h) DBP Blast #15, (i) SBP Blast #16, (j) TBP Blast #8, (k) DBP Blast #30, and (l) SBP Blast #30.

Figure 6. Frequency content of blast-induced ground motions: (a) normalized Stockwell spectrogram showing variation of frequency content of the body wave components over time, (b) Fourier amplitude spectrum of particle velocity for TGP S3x during SBP Blast #10, and (c) variation of predominant frequency of *P-wave*, SV_x*-wave* (near-field) and SV_z*-wave* (far-field) during the Shallow Blast Program from two representative TGPs.

Figure 7. Dynamic response of the Silt Array including the variation of the: (a) Cauchy shear strain, γ_{xz}, (b) octahedral shear strain, γ_{oct}, and (c) excess pore pressure ratio, r_u, time histories for the Deep Blast Program, and the: (d) γ_{xz}, (e) γ_{oct}, and (f) r_u time histories for Shallow Blast Program.

Figure 8. Example of Cauchy shear strain, γ_{xz} and corresponding excess pore pressure ratio, r_u, time histories observed in the Silt Array at Elements 1 and 2 for the various charge detonations during the Shallow Blast Program: (a) – (c) Element 1 (PPT-2), (d) – (e) Element 2 (PPT-3).

Figure 9. Variation of excess pore pressure, r_u, and maximum DSS-equivalent shear strain, $\gamma_{DSS,max}$, deduced for the Silt Array during the Test (TBP), Deep (DBP), and Shallow Blast Programs (SBP): (a) maximum shear-induced excess pore pressure ratio, $r_{u,max}$, and (b) residual shear-induced excess pore pressure ratio, $r_{u,r}$, with $\gamma_{DSS,max}$, and (c) comparison of $r_{u,r}$ from *in-situ* tests and intact DSS test specimens.

Figure 10. Body wave component identification and velocities: (a) example of an orthogonal, three-component velocity time history (TGP S3, #3) and (b) corresponding normalized Stockwell spectrogram (TGP S3x); and comparison of the vertical body wave amplitudes and

phases of two horizontally-separated geophones: (c) SBP Blast #3 observed in TGPs 3 and 6, and (d) SBP Blast #20 observed in TGPs 5 and 8.

Figure 11. Variation of shear wave velocity, V_s, with $\gamma_{DSS,max}$ in the Silt Array for the: (a) Test Blast Program (TBP), and (b) Shallow Blast Program (SBP); and, comparison of the: (c) measured *in-situ* shear modulus degradation and strain-controlled DSS test data for intact specimens (N = 1) with $\gamma_{DSS,max}$ and threshold shear strains identified, and (d) strain rate-corrected G/G_{max} with $\gamma_{DSS,max}$ (f = 1 Hz).

Figure 12. Effect of excess pore pressures on undrained shear strength: (a) normalized, post-cyclic, constant-volume, monotonic shear stress-shear strain response from DSS tests on natural, intact specimens, and (b) variation of post-cyclic DSS and post-blast vane shear test normalized undrained shear strength ratio with cyclic and blast-induced, *in-shear* maximum excess pore pressure ratio.